

Diplomarbeit

Carrier Lifetime Improvement in 4H-SiC by Thermal Oxidation

ausgeführt zum Zwecke der Erlangung des akademischen Grades
Master of Science

unter der Leitung von

Dipl.-Ing. Ian Booker und Prof. Dr. Gottfried Strasser

Institutionen för fysik, kemi och biologi, Linköpings Universitetet und
Institut für Festkörperelektronik, Technische Universität Wien

eingereicht an der Technischen Universität Wien,
Fakultät für Elektrotechnik und Informationstechnik

von

Hassan Abdalla

Matrikelnummer: 0625282

Wendstattgasse 4/31/7
1100 Wien, Österreich

Wien im Jänner 2014

Zusammenfassung

Im Zuge der Forschung an Siliziumkarbid (SiC) der Halbleitermaterialien Gruppe des IFM an der Universität Linköping, wurden die Einflüsse von thermischer Oxidation von 4H-SiC auf die Ladungsträgerlebenszeit untersucht und die Ergebnisse mit vorhandenen Modellen in Verbindung gebracht [34]. Die vorliegende Arbeit veranschaulicht den Einfluss der Oxidationsparameter wie Oxidschichtdicke, Oxidationstemperatur und Oxidationszeit auf die Ladungsträgerlebenszeit verschiedener Proben [9]. Zusätzlich wurde der Einfluss verschiedener Anfangsbedingungen während des Aufheizens in einem Al_2O_3 , sowie einem induktiv beheizten Quarzofen untersucht. Es wurde gezeigt dass die Diffusion von Natrium des Al_2O_3 Ofen einen starken Einfluss auf die Wachstumskinetik des Oxids hat [2].

Photolumineszenz (PL) sowie zeitabhängige PL (TRPL) wurden zur Bestimmung und Charakterisierung der Lebenszeiten der Minoritätsladungsträger benutzt, während deep level transient spectroscopy (DLTS) zur Untersuchung und Konzentrationsbestimmung tiefliegender, nichtstrahlender Rekombinationszentren benutzt. Zur Unterstützung der Charakterisierung wurden die Ergebnisse aus diesen Untersuchungen mit theoretischen Simulationen basierend auf der Arbeit von Klein et. al [34] verglichen.

Die hier präsentierten Ergebnisse weisen auf zwei neue Defekte bei 370K und 460K mit ungewöhnlichen Eigenschaften und durch $Z_{1,2}$ unerklärlichem Lebenszeitverhalten hin, welche in einer nachfolgenden genaueren Analyse als $\text{ON}_{1,2}$ identifiziert wurden. Es wurden verschiedene Annahmen getroffen um das Verhalten und die Herkunft dieser Defekte zu erklären. In jedem Fall geben die Ergebnisse Anlass zur weiteren Untersuchung besagter Defekte.

Abstract

Implemented in the ongoing research of the semiconductor materials group at the IFM at the university of Linköping on SiC, effects influencing the carrier lifetime as a result of thermal oxidation of 4H-SiC have been investigated and correlated with existing models [34]. This work presents the influence of the oxide parameters such as layer thickness, oxidation temperature and time [9] on the carrier lifetime of different as-grown samples. In addition, the influence of various initial conditions during the preheating process in two different oxidation furnaces on carrier lifetime are presented. One is an Al_2O_3 tube furnace and the other is an inductively heated quartz tube furnace. Of interest here is that doping of the oxide with Na from the Al_2O_3 furnace have been shown to have a strong influence on the oxide growth kinetics [2].

Photoluminescence (PL) and time-dependent PL (TRPL) have been used to determine the minority carrier lifetimes and deep level transient spectroscopy (DLTS) was used to investigate the deep-lying non-radiative combination centres and determine their concentration. The results have been compared to a theoretical simulation based on the work of Klein et al. [34] to aid with characterization.

The results presented here indicate the presence of two new defects at 370K and 460K, later identified as $\text{ON}_{1,2}$, with peculiar properties and a general lifetime behavior which cannot be explained by $\text{Z}_{1,2}$ alone. Several assumptions regarding the properties of these defects have been made based on the experimental findings in an effort to explain their origin and suggest further investigation of said defects.

Contents

1	Introduction	1
2	Silicon Carbide	3
2.1	Structure and Polytypes	3
2.2	General Properties of SiC	6
2.2.1	Mechanical Properties	6
2.2.2	Thermal Properties	6
2.2.3	Optical Properties	8
2.3	Electronic Properties	9
2.3.1	Band Structure	10
2.3.2	Carrier Mobility	11
2.4	Carrier Generation and Recombination - Lifetime	12
2.4.1	Band-Band Recombination	13
2.4.2	Exciton Recombination	13
2.4.3	Free to Bound Recombination (Band-Impurity Recombination)	14
2.4.4	Auger Recombination	14
2.4.5	Surface Recombination	14
2.4.6	Impact Ionization	15
2.4.7	Carrier Lifetime	16
2.5	Epitaxial Growth of SiC	18
3	Defects in Silicon Carbide	21
3.1	Intrinsic Carrier Concentration	22
3.2	Point Defects in SiC	24
3.3	Deep Level Defects	24
4	Thermal Oxidation	29
4.1	Silicon and Carbon Emission Model	29
4.2	Defect Reduction by Thermal Oxidation	32

Contents

5	Characterization	35
5.1	Time Resolved Photoluminescence	35
5.1.1	Experimental Technique	36
5.1.2	Set Up	37
5.1.3	Temperature Dependent TRPL	38
5.1.4	Injection Level Dependent TRPL	38
5.2	Deep Level Transient Spectroscopy	38
5.2.1	Contacting	39
5.2.2	Experimental Technique	40
5.3	Doping Density	44
6	Simulation	47
7	Experimental Series	49
7.1	Experimental Details	53
7.2	Increase in Minority Carrier Lifetime by Thermal Oxidation	54
7.3	PL Spectra and TRPL	60
7.4	Deep Level Transient Spectroscopy	67
8	Conclusion	75
	List of Figures	80
	List of Tables	81
	References	88

Introduction

Even though the electrical properties of Silicon Carbide (SiC) have been discovered as early as 1907 in the form of light emission from a SiC crystal under application of an electric field [56], it was mainly used as a material for abrasive tools, due to its hardness and high decomposition temperature of around 2700°C. It was not until the 1970's that its electronic potential has been exploited and its properties researched. Owing to its unique properties SiC, as a semiconductor material, has become subject to active research. Being able to withstand higher operation temperatures and levels of radiation in addition to having a higher electrical break down field resulting from a wider band gap, SiC can replace common materials like Si or GaAs in electronic applications which operate at high frequency and/or voltage and in harsh environments. In addition to the already mentioned properties, increasing availability of larger wafers, the ease with which it is possible to grow epilayers without lattice mismatch on native substrates and good dopability make SiC an especially favorable choice for devices such as Schottky diodes, MOSFETs and bipolar transistors.

The oxidation of SiC is used in MOS devices with operating temperatures as high as 650°C [49] where the channel-forming oxide is grown on top of the SiC layer. The detailed oxidation mechanisms, however, are not fully understood and the electrical properties of SiO₂ are far behind the predictions from theoretical models based on the oxidation mechanism of Si [67]. These limitations, which prevent SiC-oxide-devices from being used in a larger scale, are usually credited to defects at the SiC/SiO₂ interface [67]. Although not topic of this thesis, it is of utter importance to gain a deeper knowledge of the mechanisms and oxidation parameters that influence the quality of the oxide, when using an oxide layer as part of a device. Furthermore, it has been shown [23] that oxidation of SiC has a lifetime increasing effect on the minority carriers in the epilayer on which the oxide is formed. Being able

to adjust the lifetime of minority carriers to ones specific needs is an important tool to have when designing bipolar devices. If the lifetime is too short, the voltage drop across the diode is high and in addition an increase in leaking current becomes present, when operating the diode in reverse mode. A too large lifetime, on the other hand, allows for a better conductivity but also slows down the switching frequency. The mechanism behind the lifetime increasing effect of thermal oxidation is discussed in numerous papers [29, 20, 22, 23, 67, 9, 37] and no detailed physical model which can describe the observed effects has been suggested to date. Nevertheless, it is believed that the formation of carbon interstitials, created by emission from the epilayer surface during oxidation, diffuse into the epilayer and recombine with the so-called $Z_{1/2}$ deep levels which are believed to be single carbon vacancies in the crystal [34].

In this thesis I will concentrate on the lifetime enhancing effect of thermal oxidation of 4H-SiC, rather than the electrical properties of the oxide itself. The choice for the 4H type of SiC follows from its superior electrical properties, like high carrier mobility along the vertical axis, which is beneficial for vertical devices such as Schottky diodes as well as the great amount of research that has already been done on 4H-SiC, thus making it easier to compare results and draw reasonable conclusions.

Silicon Carbide

SiC is a IV - IV compound with semiconducting properties. An interesting feature of SiC is the vast amount of crystallographic modifications, referred to as polytypes [66], which can be obtained. They can be identified by means of X-ray diffraction [28].

The basic building blocks for every polytype are Si-C-bilayers (Fig.2.1), which are stacked in a sequence that repeats itself after a number of layers, specific for every polytype. The different stacking sequences of the bilayers have great influence on the electronic and mechanical properties. Although more than 200 different polytypes of SiC have been identified [66], only very few are stable and can be synthesized with satisfying quality without mixing of polytypes. Nevertheless, precise control of the temperature gradient in the growth system and progress in wafering make available single crystal wafers of up to 100mm in diameter with a very low defect density [41], thus introducing them to a greater market in the industry. In the following section the different polytypes and their properties will be described briefly, followed by a brief description of SiC growth.

2.1 Structure and Polytypes

The basic unit of SiC consists of four Si atoms at the corners of the tetrahedral unit cell bonded to one C atom in the middle or 4 C atoms on the corners and one Si atom in the middle of the tetrahedral arrangement (Fig.2.1(a)).

The bonding between the Si and the C atoms is of the covalent type and constituted by sp^3 -orbital hybridization. Charge density calculations conclude that the bonding shows also ionic characteristics (network covalent) [50], [12]. The equilibrium bond length is 1.89Å between two atoms of different kind and 3.09Å between two equivalent atoms [51].

The basic building block of every polytype is the bilayer. To form a bilayer, the basal plane of the tetrahedral unit cell is repeated with the dangling Si- and C-bonds periodically facing upwards and downwards (Fig. 2.1(b)). The SiC bilayer can also be thought of as a monolayer of C-atoms followed by a layer of Si-atoms.

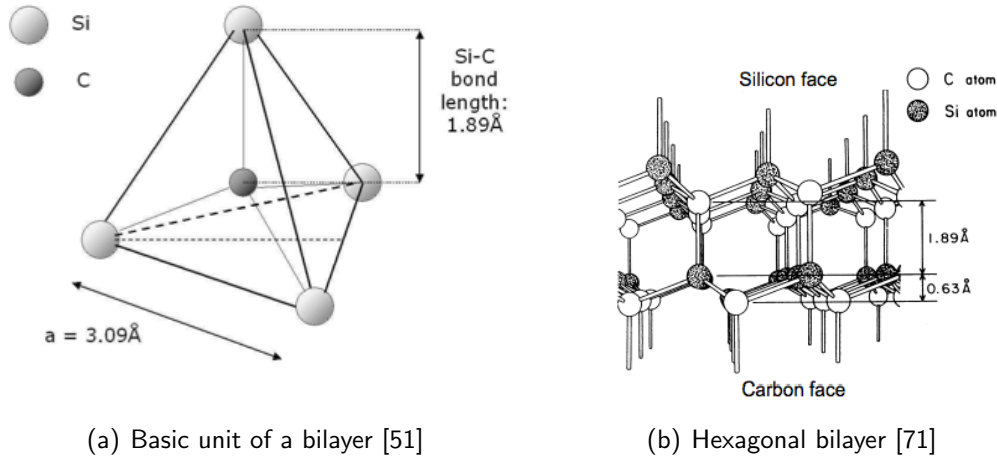


Figure 2.1: Si-C Bilayer

The bilayers are hexagonal close packed. They are stacked on top of each other along the natural direction of growth, the (111) direction for cubic structure or (0001) direction for hexagonal structures. Resulting from the two possible mutual rotations between the layers to continue tetrahedral arrangement, 60° or 180° , different crystal structures arise, which are commonly described in terms of Ramsdell notation in the form of n for the number of bilayers in the unit cell, followed by the symbol for the symmetry (C for cubic, H for hexagonal and R for rhombohedral).

A rotation of 60° results in a zincblende structure with a cubic symmetry, denoted by 3C (historically also called β -SiC). This is the only possible purely cubic SiC-polytype. A 180° rotation between each layer gives a wurtzite crystal structure with a hexagonal symmetry, denoted by 2H, which is not naturally stable. Polytypes of higher order, like 4H or 6H are a mixture of zincblende and wurtzite but their overall symmetry is still hexagonal [4]. 4H and 6H are stable hexagonal modifications of SiC and widely used in research and industry. In addition, rhombohedral polytypes have been reported (the latter two polytypes are sometimes also referred to as α -SiC).

An overview of the stacking sequence of the most common polytypes is given in Fig. 2.2 In the cubic structure the stacking is repeated every three bilayers $ABC(AB\dots)$.

The most simple hexagonal structure is 2H where stacking occurs in opposite direction after every second bilayer, leading to a $AB(AB\dots)$ sequence.

The stacking sequence of 4H-SiC is $ABCB(AB\dots)$, two bilayers of equal direction are

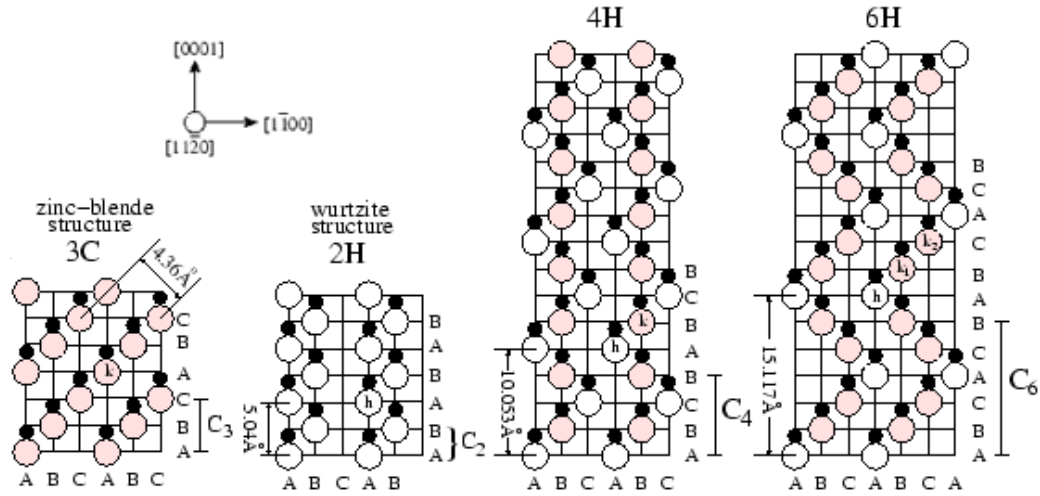


Figure 2.2: Stacking sequence of 3C, 2H, 4H and 6H in the $[1120]$ plane from [4]

followed by two bilayers of opposite direction and for the 6H-SiC polytype, sets of 3 bilayers are stacked on each other with opposite directions, resulting in the sequence $ABCACB(AB\dots)$. As can be seen from Fig.2.2 the zig-zag line, representing the chain of Si-C bonds, changes direction every time there is a change in the mutual orientation of the bilayers. The smallest stable rhombohedral modification is 15R with 15 bilayers stacked in the sequence $ABCACBCABACBCB(AB\dots)$ [66].

A satisfying explanation for the large amount of stable polytypes has yet to be found. There are two general types of approaches to explain the mechanisms behind. In short, one approach claims that the thermodynamically stable short-period polytypes act as building blocks for larger polytypes. The other refers to the growth mechanism of long-period polytypes around screw dislocations [7].

Looking at the tetrahedral bilayer unit in Fig.2.1(a), one can see that there are two ways the carbon atom can be bound to the Si atoms in c -direction. With the tip of the tetrahedron facing up, in the $(000-1)$ direction, the carbon atom binds to one silicon atom, while in the other direction with the tip facing down, (0001) , the carbon atom binds to three silicon atoms. The different number of bindings of the carbon atom to the silicon atom(s) results in different chemical properties, for example their oxidation behavior, which will be discussed in chapter 4 and is referred to as carbon- and silicon-face, respectively.

A feature shared among all wurzite polytypes is their polarity along the c -axis. In crystallographic terms, polarity is the generation of an electric field by spontaneous polarization P (or ferroelectricity). Due to the deviation of the real charge distribution from the point charge model of the ideal wurzite structure a relative shift of atoms with different electronegativities occurs, creating macroscopic polarization charges in

the bulk and fixed charges at the surfaces to compensate the bulk charges, since the crystal must be neutral in the whole. This results in a large macroscopic electric field E in the crystal following the relationship $E = P/\epsilon(\epsilon_0 - 1)$ with ϵ and ϵ_0 being the absolute and vacuum permeability, respectively [18], [52]. Polarity is not found in the zincblende structure due to the higher lattice symmetry of this structure.

2.2 General Properties of SiC

The physical properties of SiC vary depending on the concerned polytype. All hexagonal polytypes show very different lattice constants c (in c -direction) but almost the same constant a (along the side of the hexagon). As a result, also the density is different for every polytype, but is higher than the density of Si in all modifications.

Another important property shared by all modification of SiC is its crystallographic anisotropy. The elastic constants, the thermal conductivity and expansion coefficients, amongst others, show strong dependencies on the direction in which they are measured (see table 2.1). The anisotropy of SiC is generally higher than for Si, because of the hexagonality in the SiC structure (except the cubic 3C-structure) which results in less crystallographically equivalent directions in the unit cell than Si which has cubic symmetry.

SiC is chemically inert due to the strong covalent bonding between its constituents and the short bond lengths compared to other semiconductor materials.

An overview of some of the properties of SiC can be found in table 2.1.

2.2.1 Mechanical Properties

SiC exhibits a very high hardness of 9.2 to 9.3 on the Mohrs scale [17]. The elastic constant C is in general about one order of magnitude higher than for Si [24]. It ranges from 52 to 553 GPa depending on the concerned polytype (although the values for 4H- and 6H-SiC are the same within experimental uncertainties) and crystallographic direction [33]. These properties extend the use of SiC beyond semiconductor materials to ceramics for abrasive tools and protective coatings to increase the lifetime of components.

2.2.2 Thermal Properties

Among the thermal properties of SiC, especially thermal conductivity and expansion are of great interest for the design of electrical devices. Long term operation at high temperatures as well as fast changes between high and low temperatures put a lot of stress on the device and can lead to failure when the thermal properties are not known well enough. Therefore, since the early days of SiC-research, a lot of effort was put

Property	Si	H-GaN	4H-SiC	6H-SiC
Symmetry Group				
Lattice constant a [Å]	5.431	3.189	3.073	3.073
Lattice constant c [Å]	5.431	5.186	10.053	15.08
Stacking sequence	-	ABAB	ABAC	ABCACB
Mohr's Hardness	7	9	9	9
Bulk modulus B_0 [GPa]	97.6	144	217 - 224	204 - 231
Thermal conductivity λ [$Wcm^{-1}K^{-1}$]	1.3	1.2	5	5
Thermal expansion coefficient α [$10^{-6}K^{-1}$]	35	144	2.391 - 4.68	2.478
Density ρ [gcm^{-3}]	2.329	300	3.211	3.211 - 3.249
Commercial wafer diameter as of 1999 [cm]	30	15	5	5

Table 2.1: General Properties of Si, GaN and various polytypes of SiC. Data taken from [17], [50], [19], [33]

into determining and understanding its thermal properties and the mechanisms behind [61], [11], [72], [50].

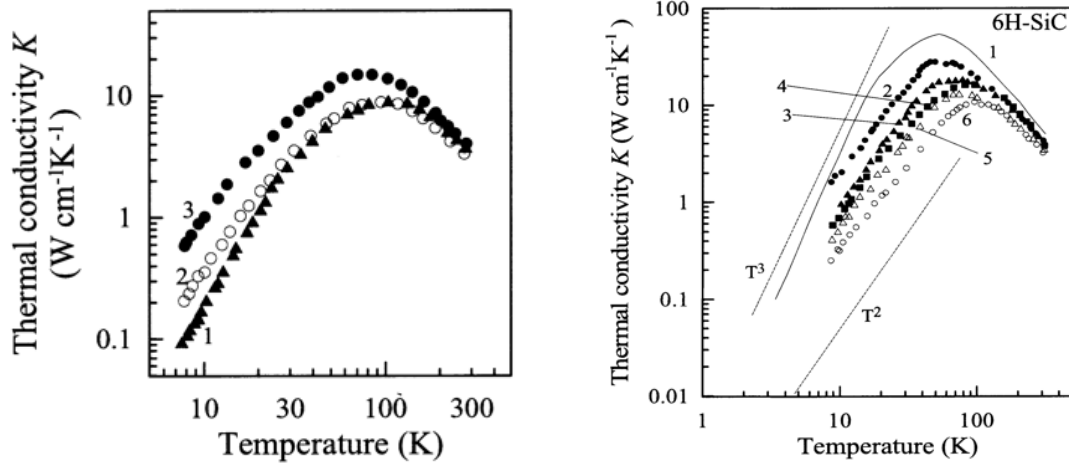
The very high thermal conductivity and low intrinsic carrier concentration of SiC allows it to maintain its electrical properties to temperatures of over 300°C [30], while Si can not be operated above 200°C.

The temperature dependence of the thermal conductivity for various polytypes is shown in Fig.2.3(a). It can be seen from Fig.2.3(b) that the thermal conductivity for the 4H and 3C polytypes show a T^3 dependence for lower temperatures, resulting from the scattering of phonons at grain boundaries, whereas the thermal conductivity for 6H is proportional to T^2 , which is characteristic for phonon scattering by electrons as seen in Fig.2.3(b). When the electron concentration increases, a decrease of κ is observed and the low temperature arm approaches a T^2 behavior [46].

In summary it can be said that the thermal conductivity depends on the temperature, the amount of impurities (carrier concentration) and the polytype. However, in general it can be said that the thermal conductivity parallel to the c-axis is about 30% lower than perpendicular to it. This can be attributed to the nature of the SiC-lattice [11].

For the fabrication of high temperature devices it is important to know the differences between the thermal expansions coefficients of the various layers in the device. This allows to calculate the mechanical stress in a temperature cycling process and account for that in the design of the device.

The thermal expansion coefficients parallel and perpendicular to the c-axis, α_{11} and α_{33} , respectively, are approximately the same for every polytype [3]. They show temperature



(a) Thermal conductivity κ vs. temperature normal to the c-axis. Curves 1, 2 and 3 represent the polytypes 4H, 3C and 6H, respectively. [45]

(b) Temperature and electron concentration dependence of the thermal conductivity κ normal to the c-axis for 6H-SiC. The electron concentration increases from very pure curve 1, to a value of $3 \times 10^{18} \text{ cm}^{-3}$ curve 6 [45]

Figure 2.3: Temperature dependence of the thermal conductivity

dependences which can be described with second order polynomials. Values for α_{11} and α_{33} of different polytypes can be found in table 2.1.

2.2.3 Optical Properties

Due to the indirect band gap of SiC, it is not very suitable for light emitting diodes. Nevertheless it was used as a light-emitter in the blue and UV spectrum until the 1980s, before the large scale development of GaN-LEDs, which emit light with much higher efficiency, rendered them obsolete.

SiC is, however, used as a material for photodetectors in the UV-range. Because of their wide band gap, such SiC photodiodes are blind to visible and infrared light, which decreases signal and background noise. This also means less leaking current, which increases the sensitivity. This advantages combined with the high thermal conductivity and resistivity against heavy radiation makes SiC a good choice for astronomical and terrestrial sensor applications [70].

2.3 Electronic Properties

Some of the main reasons for the superior electronic properties of SiC (especially at high temperatures) over Si is the wide band gap and low intrinsic carrier concentration (carrier concentration of the undoped crystal). With an increasing band gap, the thermal energy needed to lift a carrier from the valence band to the conduction band rises, thus allowing higher operating temperatures.

While at normal operating temperatures the conductivity is controlled by the artificially introduced carriers via doping, the number of intrinsic carriers increases with increasing temperature. This affects the operation of a semiconducting device in a way as to decrease the blocking voltage and increase the leaking current up to the point where the intrinsic carrier concentration is greater than the doping concentration and the device loses its semiconducting characteristics, thus becoming an ohmic resistance.

Another crucial parameter for device performance is the breakdown-field. It is proportional to voltage needed to reduce the size of the depletion layer to a value low enough to allow uncontrolled conduction in the reverse direction of a p-n junction.

Like the physical properties, the electronic properties are different for every SiC modification. Especially the size of the band gap and the intrinsic carrier concentration change among the polytypes. From table 2.2 it becomes clear why 4H-SiC is the preferred material of choice for various kinds of transistors and diodes. Its intrinsic carrier concentration (see section 3.1) is orders of magnitude lower compared with the other polytypes and of course pure Si. It also exhibits a large band gap.

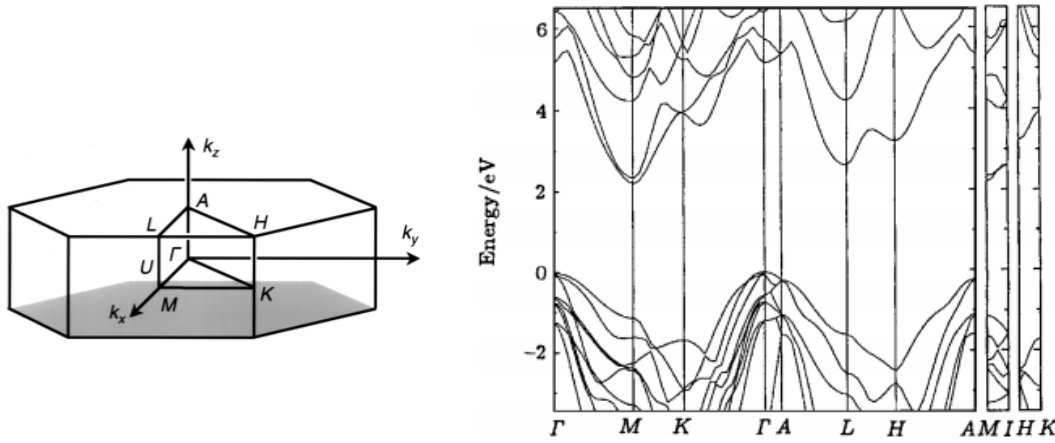
Property	Si	GaN	4H-SiC	6H-SiC
Band gap [eV]	1.16	3.39	3.26	3.03
Breakdown field [$10^6 V cm^{-1}$]	0.3	5	3	2.5
Intrinsic Carrier Conc. []				
Electron mobility [$cm^2 V^{-1} s^{-1}$]	1450	1000	950	415
Hole mobility [$cm^2 V^{-1} s^{-1}$]	450	35	115	90
Dielectric constant ϵ_r	11.7	8.9	10	9.7
Saturation drift velocity [$10^7 cm s^{-1}$]	1	2.5	2.2	2

Table 2.2: Electronic Properties of Si, GaN and various polytypes of SiC. Data taken from [17], [50], [19], [11]

2.3.1 Band Structure

The picture of the band structure is formed in the \vec{k} -space (reciprocal space), where the energy is plotted over the impulse vector \vec{k} . In Fig.2.4(b) an example of the calculated band structure of 4H-SiC in the first Brillouin zone is shown.

The first Brillouin zone (or just Brillouin zone) is the primitive elementary cell (unit cell with the smallest possible volume) in the crystal lattice in \vec{k} -space. All information about the properties and shape of the band structure in the whole crystal is confined in this zone by folding back the other zones into the first BZ. The various points with high symmetry in the Brillouin zone are denoted with roman letters and the paths connecting the points with greek symbols. In Fig.2.4(a) the Brillouin zone of the hexagonal structures is depicted. Usually the band structure is plotted along various directions of the first Brillouin zone.



(a) First Brillouin zone for a hexagonal structure. Points of high symmetry (critical points) are denoted with letters [27]. (b) band structure for 4H-SiC calculated by means of the local density theory in the local density approximation. The calculated band gap differs from the experimental value by about 30% [68].

Figure 2.4: Hexagonal Brillouin zone and band structure of 4H-SiC.

The band gap is the energy difference between the maximum of the highest valence band, denoted E_V and the minimum of the lowest conduction band, E_C , and therefore the energy necessary to lift an electron into the conduction band, which then leaves a hole in the valence band. A full valence band cannot conduct electricity and therefore the jump of the electron into the conduction band is necessary to allow conduction. In a single crystal, an electron feels a periodical potential, which shapes the band structure and is created by the periodically arranged ion cores and all the other electrons.

If the minimum of the conduction and the maximum of the valence band are at the same point in the reciprocal space, the band gap is called *direct band gap*, which means that when recombination of electrons and holes occurs, the \vec{k} remain the same. Whereas in an *indirect band gap*, the minimum and maximum are located on different points in the reciprocal space. In order for recombination to occur, the \vec{k} must change. This makes materials with indirect band gaps less suitable for light emitting purposes. All polytypes of SiC have indirect band gaps with band gap sizes varying from 2.3 eV to 3.3 eV (at 300K) [50]. It is, however, possible to transform the indirect band gap of undoped 3C-SiC into a direct band gap by means of doping with nitrogen [43], which, in turn, also shrinks the size of the band gap.

Theoretically, an intentional mixing of polytypes allows to adjust the band gap and estimations predict a rather high electron mobility at room temperature [7]. However, this has yet to be experimentally proven.

The band gap energy changes considerably with temperature due to changes in the interaction of the electrons with the expansion and contraction of the crystal lattice. This change of the band gap with temperature depends on the thermal expansion coefficient α and the volume compressibility β .

Calculating the band structure is a serious many-body problem which can be partially solved by means of the local density approximation (LDA) in the functional density theory (DFT) for which many variations exist. A typical drawback of this model is that the calculated band gap values are usually 30% below the experimentally observed values.

Experimentally, the band structure can be obtained with ballistic electron-emission spectroscopy (BEES) or photoluminescence.

2.3.2 Carrier Mobility

The carrier mobility μ describes the ability of a charge carrier to move under the influence of an electric field. The resulting carrier velocity is termed drift velocity. A higher mobility results in better electrical properties of semiconductors and is therefore desirable.

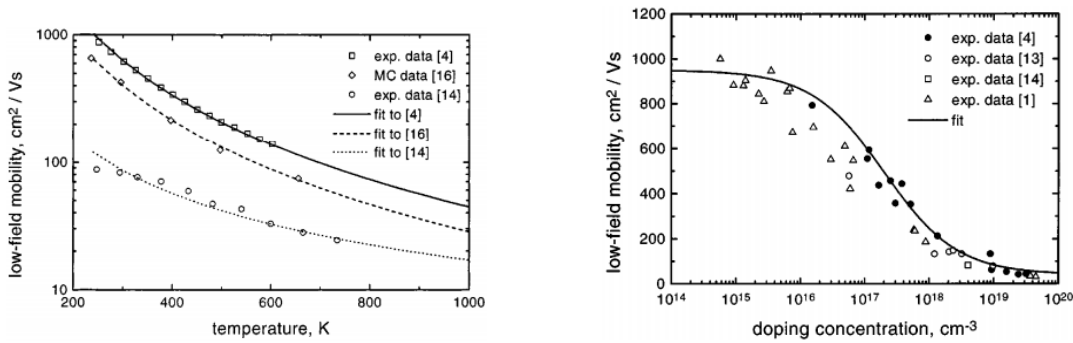
By definition, electrons have a negative mobility and holes a positive one and in the case of SiC the numerical value for electrons is almost always higher than for holes, therefore it is better to create n-type drift regions than p-type regions[5].

In SiC, the carrier mobility is dependent on the amount of doping, carrier concentration, the type of doping atoms as well as the polytype and temperature. In intrinsic crystals the mobility is limited by scattering processes of the carriers with the crystal lattice, whereas in doped materials μ is governed by the scattering at defects caused by doping or impurities.

There are generally two types of regimes to consider. In the low-field regime, which is present at small electric fields, the carrier velocity is proportional to the electrical field

and scattering processes are elastic. The mobility is then mainly dependent on the temperature and the doping concentration [55]. At high fields on the other hand, the carrier energy becomes larger than the energy of the lattice and they transfer energy to the lattice, thus reducing their drift velocity. The highest achievable velocity is called drift-saturation velocity

Fig2.5 shows the temperature and doping concentration dependence of the electron mobility in 4H-SiC. The carrier mobility is usually measured by means of Raman spectroscopy or Hall effect measurements. Additionally a lot of work is done to understand the mechanisms behind the dependencies of the carrier mobility (mainly the electron mobility), by deriving models from experimental data and data from Monte Carlo simulations [55]



(a) Temperature dependence of the low-field electron mobility in 4H-SiC. Squares and the dashed line represent experimental data and the respective fit from [57]. Diamonds and the dashed line represent Monte Carlo data and respective fit from [25] and circles and the dotted line represents experimental data and the respective fit from [32].

(b) Dependence of the low-field electron mobility on the doping concentration in 4H-SiC at 300K. The full circles and the open circles represent experimental data taken from [57] and [47] respectively. Open triangles and squares are experimental values from [26] and [32] respectively. The full line represents the fit according to the formula in [55].

Figure 2.5: Temperature and doping concentration dependence of the electron mobility in 4H-SiC from [55].

2.4 Carrier Generation and Recombination - Lifetime

The generation of electron-hole pairs in a semiconductor can be achieved by exciting the bound carriers in the valence band. This is done either by irradiating the semiconductor with an electron or particle beam, absorption of light with an energy greater than the band gap energy or injection with carriers through a contact. At high electric fields it becomes also possible to create free carriers from a collision with other carriers, this

process is called impact ionization.

Whichever way it is done, when there is no more excitation source the electrons which have been excited into the conduction band relax back to the valence band in several different ways and under release of different forms of energy, this process is called recombination.

There are several different mechanism for recombination to occur, depending on the semiconductor material as well as the impurity concentration and kind. They differ in magnitude and form of energy released during the recombination process. Important recombination mechanisms are shown in Fig.2.6 and explained in the following. The processes in Fig.2.6 are for direct semiconductor, but the same principle holds true for indirect semiconductors with the difference that a third partner is needed for the recombination to happen.

2.4.1 Band-Band Recombination

In the Band-Band recombination an electron from the conduction band relaxes directly to the valence band, where it recombines with a hole. In direct semiconductors this process usually is radiative, whereas in indirect semiconductors, such as SiC, the electron requires the help of a phonon to make an optical transition across the band gap, which is less probable. This results in a weaker photoluminescence (PL) signal for indirect semiconductors.

2.4.2 Exciton Recombination

Instead of relaxing directly from the conduction band to the valence band, an electron can recombine with a hole via intermediate steps. An electron and a hole can bind and form a quasi-particle with a certain binding energy called exciton before recombining with each other.

If the electron and the hole are not localized somewhere in the band structure, the exciton can move freely in the lattice and is therefore referred to as free exciton. Free-exciton recombination is mainly observed at low temperatures for semiconductors with small binding energies (like SiC or GaAs), but can also be observed at room temperature for high binding energies (ZnO). The energy values from a such a PL measurements can be used to characterize the polytypes of SiC.

If an electron-hole pair localizes at a trap, such as impurities or defects, the resulting bound complex formed before recombination is called bound exciton. Bound excitons are formed either by sequential capturing of an electron and a hole or the capture of a free exciton. The excitons can be bound to neutral or ionized defects (donors and acceptors). The most common dopants for SiC (Nitrogen, Phosphor, Aluminum, Beryllium and Gallium) are known to bind excitons.

2.4.3 Free to Bound Recombination (Band-Impurity Recombination)

In the free to bound recombination, the carriers are captured by impurities. An electron from the conduction band recombines with a hole bound in an acceptor, the same applies to a hole in the valence band and a donor. It is the inverse process of supplying carriers from an impurity to a band. The kinetics of this process are describe in the theory of Shockley-Read-Hall (section 2.4.7).

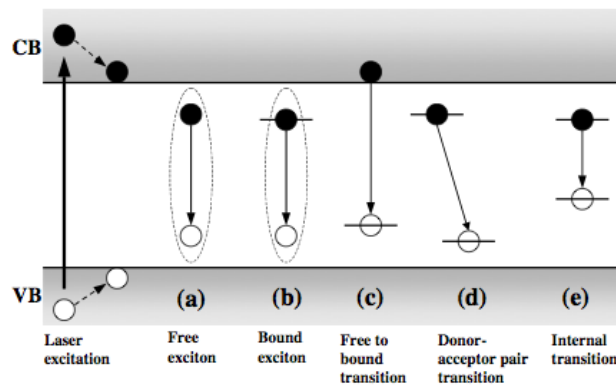


Figure 2.6: Various recombination processes depicted in a simple band model.

2.4.4 Auger Recombination

All of the previously discussed recombination processes are of radiative nature and in competition with the Auger recombination, where the energy released during the recombination of electrons and holes is not transferred by a photon, but by a third particle (electron or hole). The third particle eventually transfers its energy to the lattice via phonon emission. Since it is a three particle process it is more likely to occur for high carrier densities, high injection levels or small band gaps.

2.4.5 Surface Recombination

Dangling bonds at the termination of the crystal lattice as well as lattice mismatches at interfaces between the substrate and the layer grown or attached on top of it, create states in the band gap that provide recombination centers. These states exist only in a plane on the surface or interface, where the crystal structure terminates. Surface recombination can easily become the dominating influence of the measured lifetime when the surface roughness is high, e.g. after mechanical polishing or etching.

2.4.6 Impact Ionization

Impact ionization is the process of creating an electron-hole pair via collision of a carrier with high energy with a carrier of lower energy. The mechanism is similar to the inverse Auger recombination. Impact ionization is the main reason for the so called avalanche breakdown, the failure of power devices at high voltages.

At high enough electric fields an electron from the conduction band gains energy above the threshold energy for creating an electron-hole pair by colliding with an electron from the valence band, thus lifting the valence electron to the conduction band and creating the carrier pair. The same principle applies for a hole from the valence band colliding with an electron from the valence band.

Strong electric fields but also the working environment may increase the temperature of a semiconductor. As the phonon energy contributes to the energy of the carriers, the amount of carriers above the ionization threshold energy increases dramatically with temperature.

The electric field in a semiconductor device is within the depletion layer. To gather energy above the threshold for ionization, the carrier requires a certain width of the depletion layer. If the width is greater than the mean free path of the carrier, multiple ionizations occur (charge multiplication) which eventually leads to avalanche breakdown.

The generation rate G of electron-hole pairs by impact ionization is defined as the number of carrier pairs created per unit of distance traveled by the incoming carriers along the direction of the electric field and is given by [18]

$$G = \alpha_n n v_n + \alpha_p p v_p \quad (2.1)$$

where n and p are the carrier densities and v_n and v_p are the respective drift velocities. From $J_n = q n v_n$ and $J_p = q p v_p$, the current densities of electrons and holes, and eq.2.1 it becomes clear that the generation rate by impact ionization is proportional to the current density. α_n and α_p are the electron and hole ionization coefficients, respectively. They describe the creation of electron-hole pairs caused by electrons and holes.

It can be seen from eq.2.1 that a smaller value for the ionization coefficients leads to a lower generation rate and therefore to a higher breakdown field (breakdown voltage). α_n and α_p are hence meaningful constants for the breakdown field potential of a semiconductor. The ionization coefficients roughly follow the heuristically derived Chynoweth's law [13]

$$\alpha_n = A_n \exp\left(-\frac{B_n}{E}\right) \quad \alpha_p = A_p \exp\left(-\frac{B_p}{E}\right) \quad (2.2)$$

where A_n , A_p and B_n , B_p are experimental fitting parameters and E is the electric

field strength along the direction of the current flow. Because of the wide band gap of SiC, the threshold energy for impact ionization and therefore the breakdown field is much higher than for silicon. In Fig.2.7 the values for the impact ionization coefficients of Si and 4H-SiC are compared. It can be seen that the onset of carrier generation in 4H-SiC occurs at fields higher by an order of magnitude compared to Si. As a result, breakdown in 4H-SiC occurs at around $2 - 3 \times 10^6 \text{ V/cm}$. Noteworthy is that the impact coefficient in Si is greater for electrons than for holes, while for SiC the opposite holds true [5].

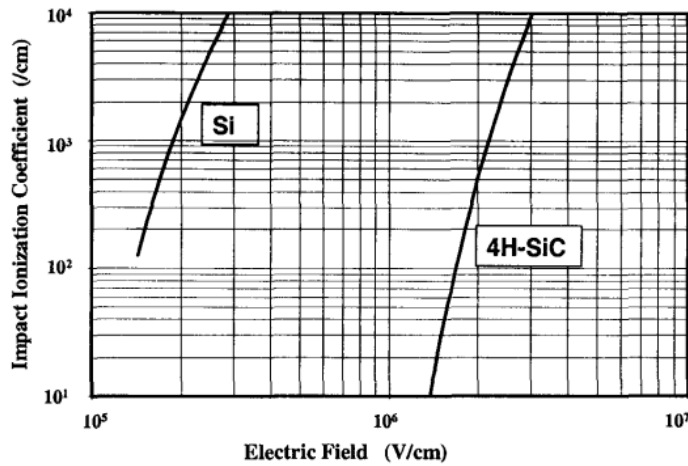


Figure 2.7: Impact ionization versus electric field strength [5].

2.4.7 Carrier Lifetime

The carrier lifetime (minority carrier lifetime) is defined as the average time it takes for an excess minority carrier to recombine or, in other words, the average time it takes to reduce the amount of carriers to $1/e$ of the excited state. Here, only n-type SiC with holes as minority carriers will be discussed, but the same principle applies for p-type SiC as long as the amount of defects is not too high.

Without any excitation a dynamic equilibrium between two processes exists. The spontaneous emission of an electron from a negatively charged trap into the conduction band represented by the left side of eq.2.3 is equal to the capture of electrons in a neutral trap, represented by the right side of eq.2.3. In this equation, e_n and c_n are the emission and capture rates, respectively, which depend on the emission property of the trap multiplied by the density of traps N_D . n_e is the number of electrons and f and f_p are the fractions of the N_D traps that are in the more negative and more positive state, respectively [59]. Equation 2.3 expresses the electron-hole pairs which

are generated and recombine constantly, while their average concentration remains the same

$$e_n f = n_e c_n f_p. \quad (2.3)$$

The equivalent expression for holes is given by

$$e_p f_p = n_p c_p f. \quad (2.4)$$

With the mass-action law $n_p n_e = n_i^2$, f and f_p can be eliminated, resulting in the detailed-balanced relationship

$$e_n e_p = c_n c_p n_i^2. \quad (2.5)$$

To arrive at an expression for the lifetime two more pairs of carrier densities shall be introduced. n_1 and p_1 are the densities for the condition at which half of the traps are in the more negative state, while the other half is in the more positive state ($f_p = f = \frac{1}{2}$). From eqs.2.3 and 2.4 these new densities follow to

$$n_1 = \frac{e_n}{c_n} \quad p_1 = \frac{e_p}{c_p}, \quad (2.6)$$

which obey the mass-action law. n^* and p^* represent the densities at a condition where electron capture and emission and hole capture and emission occur at the same rate. Inserting this condition into eqs.2.3 and 2.4 leads to the equality densities

$$n^* = \frac{e_p}{c_n} \quad p^* = \frac{e_n}{c_p}, \quad (2.7)$$

which also obey the mass-action law. An excitation of the semiconductor introduces new carriers and increases the density of majority and minority carriers to $n_e + \delta n_e$ and $n_p + \delta n_p$. The detailed-balanced relationship (eq.2.5) is therefore not valid anymore. The relative increase is much higher for the minority carriers since their density is smaller in thermal equilibrium. By definition [59], assuming a small disturbance, the steady-state minority lifetime is given by

$$\delta n_p = \tau_p g_L, \quad (2.8)$$

where the holes are generated at a rate of g_L and live for an average time of τ_p . The rate of hole capture from the extra holes is then given by $\delta n_p c_p f$. To account for holes that are re-emitted after their capture and thus must be captured again, the extra hole capture must be corrected by the effectiveness of the hole capture (which is equal to the probability that a positively charged trap becomes negatively charged by electron capture rather than hole emission) $c_n n_e / (c_n n_e + e_p)$, resulting in the total rate of recombination of electron hole pairs, which must be equal to the rate of hole

generation. The total rate of recombination follows to

$$g_L = \frac{\delta n_p c_p f c_n n_e}{c_n n_e + e_p}. \quad (2.9)$$

Rewriting the effectiveness factor in terms of n_e and n^* gives $[1 + (n^*/n)]^{-1}$. Thus, the more n-type the semiconductor, the higher the capture effectiveness. After rewriting the total rate of recombination eq.2.9 in terms of n_1 and n^* , the lifetime in eq.2.8 follows to

$$\tau_p = \frac{\delta n_p}{g_L} = \tau_{p0} \left(1 + \frac{n_1}{n}\right) \left(1 + \frac{n^*}{n}\right), \quad (2.10)$$

where τ_{p0} is referred to as the limiting lifetime with $\tau_{p0} = 1/c_p$.

2.5 Epitaxial Growth of SiC

Epitaxial growth is the process of growing an epilayer on top of a substrate of the same or different material. Two types of epitaxial growth are distinguished depending on the structure of the epilayer. If the epilayer continues the crystal structure of the substrate the process is called homoepitaxial growth, otherwise its called heteroeptiaxial growth. Amongst the various epitaxial growth methods, such as Molecular Beam Epitaxy (MBE), Liquid Phase Epitaxy (LPE) or sublimation epitaxy, chemical vapor deposition (CVD) is presently the most widely used epitaxial technique for the growth of SiC. In a CVD process, the chemical constituents, volatile precursors (in the case of SiC those are silane and a hydrocarbon gas), are introduced into the reactor with hydrogen as a carrier gas. Gaseous by-products created when the precursors react with the substrate are removed by a gas flow through the chamber. The n-dopants for SiC are introduced by volatile nitrogen. To promote the chemical reaction necessary for the epitaxial growth, the substrate is heated up to between 1450°C and 1650°C.

There are generally two types of CVD reactors known as hot wall (HW) and cold wall (CW) reactors. The main difference between those two is the temperature difference between the wall of the growth chamber and the substrate. While in a HW reactor the temperature is nearly the same in the whole chamber due to its insulation around the susceptor carrying the substrate. CW reactors, on the other hand, show a strong radial temperature gradient. As a direct consequence of the different temperature gradient, the two systems deliver epilayers of very different quality and suitability for high performance devices as investigated by Thomas et al. [65]. According to their findings, in a HW reactor the gas composition remains nearly unchanged with distance from the substrate, resulting in a more stable growth and less variation in thickness and doping compared to a CW reactor, where the gas composition changes drastically already close to the substrate. Additionally, the surface roughness of epilayers grown

in a CW reactor is about an order of magnitude larger compared to a HW reactor. Especially for device fabrication, this parameter is of great importance (interfaces) and makes epilayers grown in CW reactors unsuitable for usage in a semiconductor device.

Defects in Silicon Carbide

During the growth of a single crystal it is unavoidable that defects are introduced into the otherwise perfect lattice. These defects can be electronically and/or optically active and create defect states in the electronic structure of the crystal. The controlled introduction of defects in the form of foreign atoms into the crystal lattice, called doping, is of great importance for semiconductors, since it allows to adjust the electronic properties to ones specific needs.

In a simple model, the lowest conduction band and the highest valence band are represented by a straight line (Fig.3.1). They are separated by the band gap, which is a forbidden zone for charge carriers. Defects in the lattice create electronic states within the band gap. Depending on the kind (origin) of the defect, the position of the respective defect state within the band gap changes. In Fig.3.1 the different energy

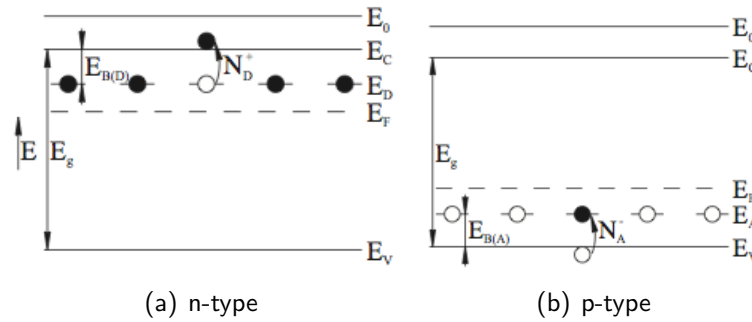


Figure 3.1: Simple band model to demonstrate the various energy positions of defect states energy bands and the Fermi level from [54]

levels are denoted by E_C , E_D , E_A , E_V and E_G for the conduction band, donor level,

acceptor level, valence band and the band gap, respectively. E_F is the Fermi level. In thermodynamic equilibrium the Fermi-level is a measure of the degree of occupation for electrons and holes, thereby determining the density of carriers in the crystal. Doping shifts the Fermi level, since it introduces additional states that can be occupied by charge carriers. The distance of the defect states from the conduction or valence band in the energy diagram corresponds directly to their thermal activation energy, also referred to as ionization energy.

In the equilibrium state, the conduction band is filled with holes (or in other words it is empty), while the valence band is filled with electrons. This leads to insulation since there is no free space for the carriers to move. In order for conduction to happen in a n-type semiconductor (Fig.3.1(a)), electrons must be excited into the conduction band, this can happen thermally, by optical absorption or an electric field. The electrons can come from the valence band, in which case they must overcome the whole band gap, or they can be excited from states containing electrons within the band gap, referred to as donator, as indicated by the arrow in Fig.3.1(a). In the latter case the energy needed to lift an electron into the conduction band is reduced by the amount of the activation energy.

In a p-type semiconductor conduction happens in the valence band. To allow conduction an electron must leave the valence band, either to the conduction band or, energetically favorable, to a defect state in the band gap that accepts electrons, referred to as acceptor. The process is schematically shown in Fig.3.1(b).

Nitrogen is usually used as a dopant in n-type SiC, while aluminum is the preferred choice for p-type SiC.

3.1 Intrinsic Carrier Concentration

In a pure, undoped crystal with no lattice defects at absolute zero ($T=0K$) the valence band is completely filled with electrons and conduction is therefore not possible. At finite temperatures, however, the electrons have a certain probability to move to the conduction band and allow for conduction to happen. These free carriers in an ideally pure crystal are called intrinsic carriers and the density of these thermally created electrons and holes is denoted by n_i and p_i respectively.

In the case of 4H-SiC this intrinsic carrier concentration is between $10^{-9}cm^{-3}$ and $10^{-7}cm^{-3}$ at $300K$ depending on the quality of the epitaxial growth [4]. This is a very low value especially when compared to other semiconductors but also compared to other polytypes of SiC.

With rising temperature, the number of intrinsic carriers increases, since the thermal energy of the lattice increases and more electrons can change to the conduction band state, thus increasing conductivity of the undoped material. Figure 3.2 shows the temperature dependence of the intrinsic carrier concentration of Si, Diamond and various

polytypes of SiC. From this, the maximal operation temperature can be estimated, which is reached when the intrinsic carrier concentration approaches the level of the intentionally introduced carriers in the doped crystal.

In an actual devices, however, other parameters like the Schottky barrier height (section 5.2.1) at interfaces and the mechanical stability at high temperatures of other materials in a device limit the maximal operating temperature to a value usually before the critical intrinsic carrier concentration is reached. The intrinsic carrier concentration

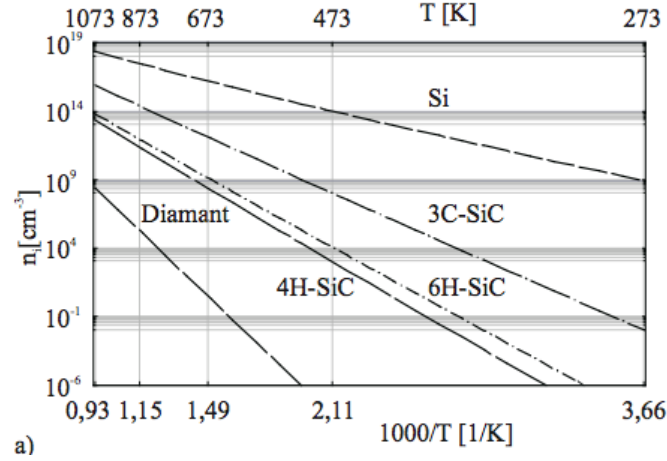


Figure 3.2: Calculated Temperature dependence of the intrinsic carrier concentration for Diamond, Si, 3C-SiC, 4H-SiC and 6H-SiC from [54]

is an important value to know for the electrical characterization of the semiconductor material, such as Deep Level Transient Spectroscopy (DLTS) and Time-Resolved Transient Spectroscopy (TRPL).

In a pure semiconductor, the amount of electrons n and holes p are the same, meaning that for every electron in the conduction band there is a hole in the valence band

$$p_i = n_i. \quad (3.1)$$

From the conduction and valence band edge density of states N_C and N_V and the band gap energy $E_G = E_C - E_V$, the carrier concentration for electrons and holes in dependence of the temperature can be obtained

$$n_i = p_i = \sqrt{np} = \sqrt{N_C N_V} e^{(-\frac{E_G}{2kT})} \quad (3.2)$$

From this relation it is clear that the intrinsic carrier concentration for SiC is several orders of magnitude smaller than for Si, simply because of the much larger band gap of SiC. Furthermore it shows that the thermal generation of carriers in the bulk material is negligible compared to the generation of carriers by introduced defect states. While in

Si the intrinsic carrier concentration reaches a critical value of about 10^5 cm^{-3} at 270°C , the concentration for 4H-SiC is still relatively low at 430°C with only $4 \times 10^7 \text{ cm}^{-3}$ [5].

3.2 Point Defects in SiC

Defects in a real crystal can have different forms and spatial distributions. In the case of SiC, defects by mixing of polytypes can also occur and present a particular problem in SiC growth. Here only point defects will be discussed in detail, since they are believed to be the source of the lifetime limiting $Z_{1/2}$ recombination centre [36]. Considering the physical structure of a point defect in a crystal lattice there are two basic types of point defects, vacancies and interstitials. From these, various related defects can form as shown in Fig.3.3. An additional atom placed in a place in the lattice where usually no atom sits leads to an interstitial. If the additional atom is of the same species as the host lattice it is called self-interstitial (Si_i or C_i) (4). For interstitial atoms of a different kind, the resulting point defect is referred to as an interstitial impurity (1). Doping introduces a foreign atom, an impurity, which is placed in a regular lattice site (2). Aluminium in a Si-site is generally used for p-type doping and nitrogen in a C-site for n-type doping. Vacancies (3) are formed by removing an atom from its position in the crystal lattice. In SiC this can either be a silicon vacancy (V_{Si}) or a carbon vacancy (V_C). If atoms of different sublattices switch places they create an antisite. In an SiC lattice two types are possible, silicon antisite (Si_C) and carbon antisite (C_{Si}). Several other point defects can form as a combination of the

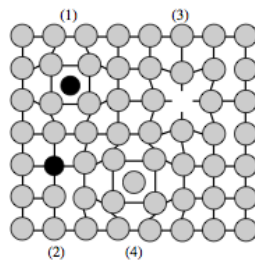


Figure 3.3: Several kind of point defects in a crystal lattice [58].

defects mentioned above. Such are Frenkel pairs, divacancies, vacancy-antisite pairs or vacancy impurity pairs, they appear in both the hexagonal and the cubic sites.

3.3 Deep Level Defects

The classification of point defects according to their energy position in the band gap separates them in to two groups, namely shallow levels and deep levels. Shallow levels

are typically created by defects with donor or acceptor states due to loosely bound electrons or holes around them. They can be well described within the effective mass theory, assuming that the carriers are screened by a coulomb potential due to the charged core of the defect. The wavefunction of the carriers in a shallow level is strongly delocalized and extends over several hundred neighbor atoms. Deep levels on the other hand, show a very localized wavefunction that decays exponentially with distance. Unlike the coulomb potential of shallow levels, the potential of a deep level can be considered as a rectangular quantum well. Deep levels can be described using the tight binding model, but no analytical solutions exist. Deep levels

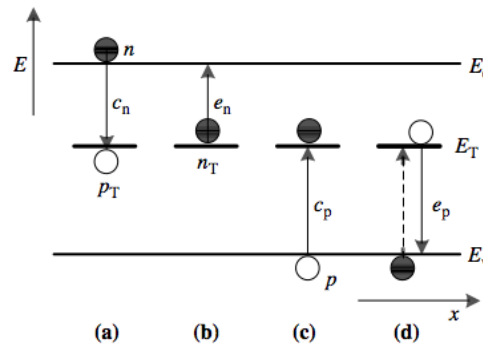


Figure 3.4: Generation and recombination of carriers via deep levels in the band gap [58].

are located close to the centre of the band gap. The exact energy position, however, depends on the occupancy of the levels within the traps with carriers. Additionally, the relaxation of the crystal lattice around the defect has influence on the energy level. Deep levels act as recombination centres when excess carriers are present and as generation centres when the Fermi-level is below its equilibrium value. The various generation-recombination processes that may occur in a deep level are depicted in Fig.3.4. Assuming the trap captures an electron from the conduction band, it can either emit the electron back to the conduction band (b) or capture a hole from the valence band (c). If the trap captures a hole, there are again two possible events that can occur. Emitting the hole back to the valence band (d) (or capturing an electron from the valence band as shown by the dashed line) or capturing an electron from the conduction band (a). A more mathematical description of the capture and emission processes is given in section 5.1.1.

It is noteworthy, however, that deep levels are not very efficient at providing free carriers but rather capture them. Hence the presence of deep levels strongly effects the conductivity of the semiconductor. Naturally, this is an undesired property in devices, which require a high minority carrier lifetime (MOSFETs) but can be beneficial for high switching devices, in which a fast removal of carriers is desired (bipolar de-

vices). In n-type 4H-SiC, two prominent electron-capturing deep level defects, $Z_{1/2}$ ($E_T \approx E_C - 0.65\text{eV}$) and $EH_{6/7}$ ($E_T \approx E_C - 1.65\text{eV}$), have been identified in DLTS measurements, with $Z_{1/2}$ being the major lifetime killer. $EH_{6/7}$ has a minor role in decreasing the lifetime because of the smaller electron capture cross section of the defect [35]. As the nomenclature suggests, each of the defects consists of similar but distinguishable defects Z_1 , Z_2 and EH_6 , EH_7 . Their microscopic nature still is a subject to discussion but experimental results suggest that they are related to carbon vacancies (V_C) [14], [9]. Annealing and DLTS measurements of 4H-SiC samples show that $Z_{1/2}$ and $EH_{6/7}$ defects are thermally stable up to 1600°C . This indicates that their macroscopic origin can not be a C_i since it is not thermally stable and would be annealed out at lower temperatures compared to V_C due to the higher mobility of C_i [8]. Furthermore, when increasing the C-level of the growth process, a decrease of $Z_{1/2}$ and $EH_{6/7}$ concentration is observed [31], thus supporting this theory. Both defects $Z_{1/2}$ and $EH_{6/7}$ show almost the same annealing and irradiation behavior, this suggest that they originate from a single V_C but in different charge states.

The broad peak of the $Z_{1/2}$ defect as shown in the DLTS spectrum in fig.3.5(b) is a result from the electronic nature of the defect, which is referred to as a negative U-center. It essentially means that the trap can capture two electrons, where the second electron is bound stronger than the first one. As a result, three possible charge states arise as depicted in fig.3.6 namely, empty, singly-occupied and doubly-occupied, leading to two possible transitions

$$Z^- \rightleftharpoons Z^0 \quad \text{and} \quad Z^0 \rightleftharpoons Z^+ \quad (3.3)$$

The possible charge states give rise to one acceptor level, Z_i^- and one shallower donor level Z_i^0 per negative U-center, where i denotes the negative U-center Z_1 or Z_2 . The reason that only one broad peak is observed during a standard DLTS measurement (section 5.2) is the freeze out of the one-electron emission. During the reverse bias pulse some of the traps are filled with two electrons, thereby increasing the binding energy of the electrons and thus making it harder for the electrons to be thermally ionized as the system returns to the equilibrium state. Consequently the observed peak in the DLTS spectra is a two-stage ionization event, where one transition is immediately followed by the other resulting in a "direct" transition from the doubly occupied Z^- state to the empty Z^+ state and hence only one peak is observed.

It is, however, possible to resolve the two peaks corresponding to the two transitions, by emptying the doubly occupied state with a light pulse and using a very short reverse pulse width to minimize the capture rate [21]. Fig.3.5 shows the distribution of the peaks when they are resolved individually (a), the single $Z_{1,2}$ transition and an energy diagram showing the negative-U property of the defect.

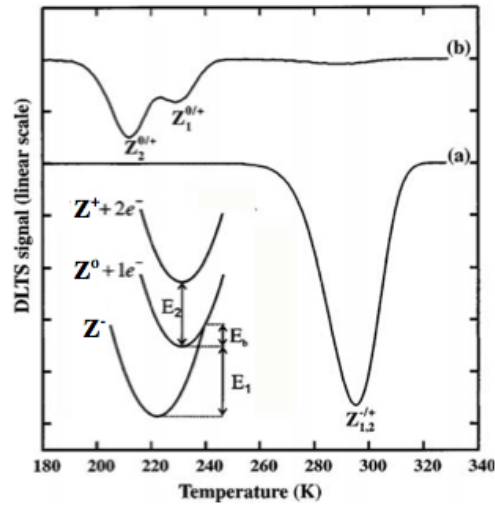


Figure 3.5: Two DLTS (see section 5.2) spectra observed in a 4H SiC diode. The measurements were performed (a) with a pulse width of $100\mu s$ and (b) with a pulse width of 50 ns and illumination with light $\lambda \approx 470\text{ nm}$ from a GaN LED before each filling pulse. The pulse height was 9.9 V and the reverse bias -9.9 V in both cases. Shown as an inset is the configuration-coordinate diagram for the center U_i where $i = 1, 2$ [21].

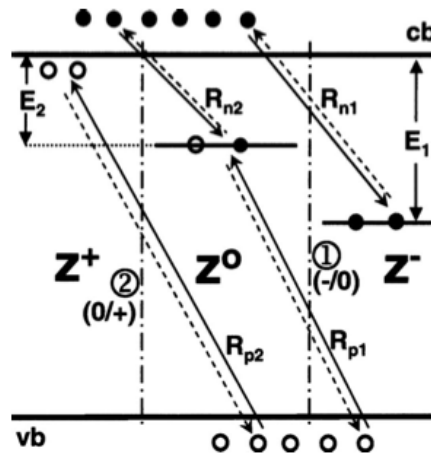


Figure 3.6: Schematic level scheme for carrier capture and emission at the $Z_{1/2}$ defect. The three charge states of $Z_1/Z_2(-, 0, +)$ are indicated, resulting in two transitions: 1 for $(-/0)$ and 2 for $(0/+)$. Transitions due to carrier capture or emission are indicated by solid or dashed arrows, respectively, with corresponding trap depths E_1 and E_2 . The net carrier capture rate for each transition is indicated by the R_{nj} and R_{pj} . [34]

Thermal Oxidation

Thermal oxidation is an established technique in Si technology to grow the insulating oxide layer on Si for MOS devices. The oxidizing agents react with the Si surface, form silicon oxide on top of it, but also consume some of the silicon wafer, thus growing in two directions.

The growth rate of the oxide layer on Si was first described by the Deal-Grove model [15] following a parabolic dependence of the oxide thickness on the oxidation time. Several corrections and additions have been made since then, like the inclusion of Si atom emission from the surface during the oxidation [44].

The electronic properties of the oxide layer in SiC MOSFETs are far behind their theoretical predictions, which is believed to be due to defects at the SiC/SiO₂. Therefore knowing the exact mechanisms of SiC oxidation is of great importance.

Thermal oxidation has been shown to have a lifetime increasing effect on SiC by decreasing the concentration of $Z_{1/2}$ and $EH_{6/7}$ traps, which are thought to be the major lifetime-reducing defects in SiC [23].

To describe the oxidation mechanism Hijikata et. al. suggested to include the oxidation and emission of C atoms to the interfacial Si emission model for Si to a model called "silicon and carbon (Si-C) emission model" [22].

4.1 Silicon and Carbon Emission Model

This model describes the growth rate of the oxide depending on the oxide thickness for the Si and the C face of SiC in good agreement with experimental results [22]. It suggests an emission of silicon and carbon interstitials from the SiC/SiO₂ interface into the oxide, where they react with the oxide. The oxide growth rate is fast initially, but decreases with longer oxidation times due to the accumulation of emitted silicon

and carbon atoms at the interface. Fig.4.1 shows the schematic mechanism of the model, where C , x and X are the concentration, distance from the interface and oxide thickness, respectively, R_1 and R_2 are the reaction rate at the oxide surface and in the oxide, respectively. The prime superscript refers to the reaction rate for C interstitials, while the subscript denotes the value for the corresponding atom.

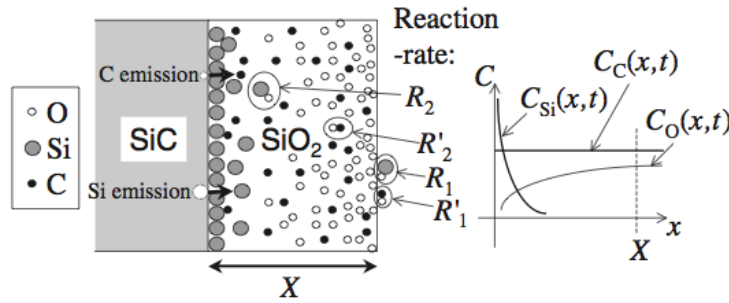


Figure 4.1: Typical DLTS Plot with majority and minority carrier traps. The height of the peaks corresponds to the trap concentration [22].

The mathematical description is based on the empirical equation for Si oxidation as suggested by Massoud et. al [44], which includes the effect of Si emission during oxidation and the oxidation and emission of C. Due to the accumulation of Si and C, the reaction rate at the interface k is a decreasing function of the concentration of the Si and C atoms and is given by

$$k = k_0 \left(1 - \frac{C_{Si}^I}{C_{Si}^0} \right) \left(1 - \frac{C_C^I}{C_C^0} \right) \quad (4.1)$$

where k_0 is the interfacial reaction rate without any accumulation at the interface, C^0 is the solubility limit of the atoms denoted in the subscript in the oxide and C^I is the concentration of the corresponding atom at the interface.

Adding terms for the Si and C emission to Fick's second law of diffusion, yields a set of equations for the diffusion of interstitials during oxidation. For C the change of concentration is given by

$$\frac{\partial C_C}{\partial t} = \frac{\partial}{\partial x} \left(D_C \frac{\partial C_C}{\partial x} \right) - R'_1 - R'_2 \quad (4.2)$$

and the change of Si concentration is given by

$$\frac{\partial C_{Si}}{\partial t} = \frac{\partial}{\partial x} \left(D_{Si} \frac{\partial C_{Si}}{\partial x} \right) - R_1 - R_2 \quad (4.3)$$

with the reaction rates R'_1 and R'_2 of the C atoms at the surface of the oxide and

in the oxide, respectively being

$$R'_1 = \eta' C_O^S C_C^S \quad \text{and} \quad R'_2 = \kappa'_1 C_O C_C + \kappa'_2 C_C (C_O)^2 \quad (4.4)$$

and R_1 and R_2 the reaction rates of Si at the surface of the oxide and in the oxide, respectively being

$$R_1 = \eta C_O^S C_{Si}^S \quad \text{and} \quad R_2 = \kappa_1 C_O C_{Si} + \kappa_2 C_{Si} (C_O)^2 \quad (4.5)$$

where η is the oxidation rate at the oxide surface, κ_1 and κ_2 are the oxidation rates of the interstitials in the oxide and "S" refers to the position at the surface of the oxide. The prime indicates that the value refers to C interstitials otherwise it refers to Si interstitials. From this, the diffusion of the oxidants follows to

$$\frac{\partial C_O}{\partial t} = \frac{\partial}{\partial x} \left(D_O \frac{\partial C_O}{\partial x} \right) - R'_1 - R'_2 - R_1 - R_2 - R_3 \quad (4.6)$$

where R_3 denotes the transportation rate of oxidants at the oxide surface. The boundary condition for these differential equations follow from the reaction equation and are given by

$$D_C \frac{\partial C_C}{\partial x} \Big|_{x=0} = -\nu_C k C_O^I \quad (4.7)$$

$$D_{Si} \frac{\partial C_{Si}}{\partial x} \Big|_{x=0} = -\nu_{Si} k C_O^I \quad (4.8)$$

$$D_O \frac{\partial C_O}{\partial x} \Big|_{x=0} = \left(2 - \nu_C - \nu_{Si} - \frac{\alpha}{2} \right) k C_O^I \quad (4.9)$$

where ν and α denote the interfacial emission rate for the corresponding atoms in the subscript and the production rate of CO, respectively. The Si-C emission model uses the results of [69] and [53], which suggest that the oxide growth rate in the thick oxide regime is proportional to the O_2 partial pressure and therefore only limited by the in-diffusion of O_2 . The oxide growth rate in this model is described as

$$N_0 \frac{dX}{dt} = (1 - \nu_{Si}) k C_O^I + \int_0^X [\kappa_1 C_{Si} C_O + \kappa_2 C_{Si} (C_O)^2] dx + \eta C_{Si}^S C_O^S \quad (4.10)$$

where N_0 is the density of Si atoms in the oxide. The first term on the right hand side describes the oxidation rate of Si atoms at the interface, the second term the oxidation of the Si interstitials in the oxide and the third term that of the Si interstitials at the

oxide surface. These equations show good agreement with experimentally obtained values in [22] as shown in fig.4.2

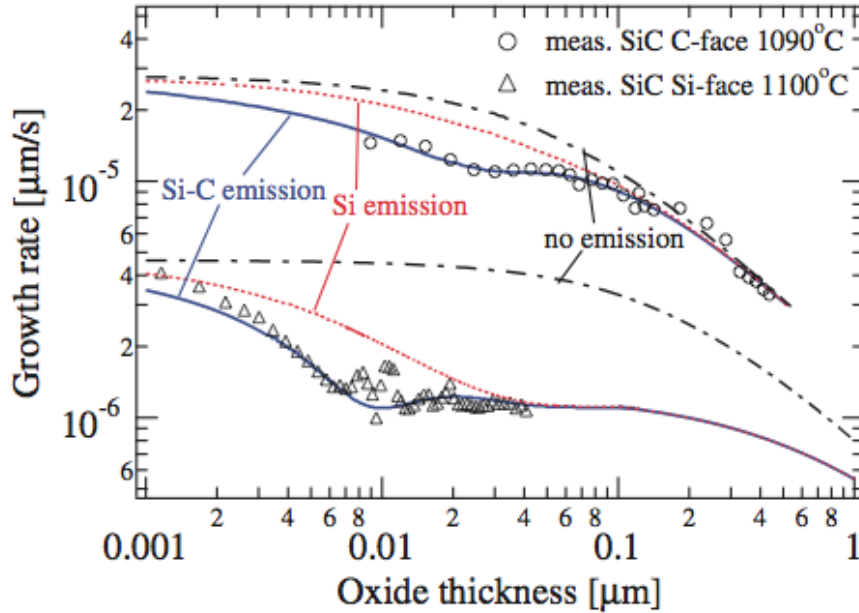


Figure 4.2: Fit of the three SiC oxidation models, Deal-Grove, Si-emission model and Si-C-emission model, to experimental results [22].

In fig.4.2 a great difference in oxidation rate between the Si-face and the C-face is visible. This can be explained by the polarity of the SiC crystal structure (see section 2.1). The emission of Si and C atoms from the surface of SiC is a result of the planar strain on the interface during oxidation.

On the C face the Si-C bond stretches along the $[0001]$ direction, resulting in very little strain to no strain in the in-plane direction during the oxidation. For the Si face, however, the bond stretches along the $[03-38]$ direction, which results in larger stress and to an increased emission of Si atoms, which greatly reduces the growth rate.

4.2 Defect Reduction by Thermal Oxidation

As mentioned in section 3.3, the prominent deep level defects $Z_{1/2}$ and $EH_{5/6}$ in SiC are believed to be related to carbon vacancies V_C . Several experiments have shown that the defect concentration can be decreased by C^+ implantation followed by thermal annealing under Ar [63], as well as thermal oxidation [23]. It is believed that this effect is due to the in-diffusion of C clusters, which form at the SiC/SiO₂ interface as a result of the C emission during thermal oxidation. These clusters recombine with the

V_C in the lattice, thus reducing the defect concentration. Additionally no experimental evidence has been found that the diffusion of C clusters creates new defects in n-type SiC [23]. The concept of this form of defect reduction is depicted in fig.4.3

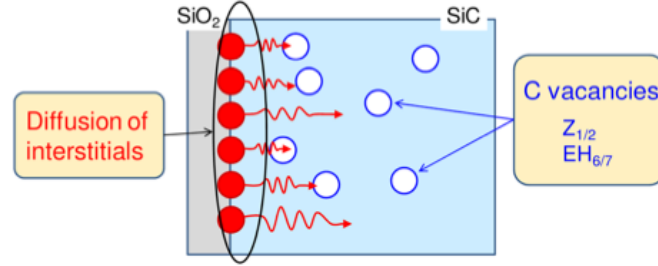


Figure 4.3: Schematic model of the mechanism behind the reduction of $Z_{1/2}$ and $EH_{5/6}$ defect concentration by thermal oxidation [29].

Based on experimental data, Kawahara et al. [29] proposed an analytical model to describe the rate and amount of defect reduction as well as the depth to which the deep levels are reduced depending on oxidation time and temperature. The C vacancies are considered to be immobile in the crystal (due to the low mobility of C_V mentioned in section 3.3) and recombine with the diffusing C interstitials. The equations describing the diffusion and recombination rates are

$$\frac{\partial n_I}{\partial t} = D \frac{\partial^2 n_I}{\partial x^2} - \gamma n_I n_V \quad (4.11)$$

$$\frac{\partial n_V}{\partial t} = -\gamma n_I n_V \quad (4.12)$$

the boundary and initial conditions are

$$-D \frac{\partial n_I}{\partial x} \Big|_{x=0} = F_0 t^{-\alpha} \quad (t \neq 0) \quad (4.13)$$

$$n_I \Big|_{t=0} = 0 \quad (4.14)$$

$$n_V \Big|_{t=0} = n_{V0} \quad (4.15)$$

the fitting parameters for diffusion, flux of interstitials and recombination of vacancies and interstitials are

$$D = D_{\infty} e^{-\frac{E_{aD}}{kT}} \quad (4.16)$$

$$F_0 = F_{0\infty} e^{-\frac{E_{aF}}{kT}} \quad (4.17)$$

$$\gamma = \gamma_{\infty} e^{-\frac{E_{a\gamma}}{kT}} \quad (4.18)$$

where n_I and n_V are the concentrations of interstitials and vacancies, respectively and γ the recombination coefficient between interstitials and vacancies. n_{V0} denotes the amount of vacancies before oxidation. The value of interstitials before oxidation can be neglected. E_{aD} , E_{aD} and E_{aD} are the activation energies for the emission of interstitials, generation of interstitials and recombination of interstitials and vacancies, respectively.

As shown in the previous section, the oxidation rate decreases with oxidation time, which means that since the flux of interstitials emitted from the surface is proportional to the oxide growth rate and therefore a decreasing function of the oxidation time t_{ox} expressed by the coefficient α . The value for α is experimentally obtained from the slope of oxide growth rate vs. oxidation time plots for different oxidation temperatures. The oxidation rate and interstitial emission are then proportional to $t_{ox}^{-\alpha}$. For simplification the oxidation rate is separated in two regimes, high-stage ($t_{ox} < 0.8h$) and low-stage ($t_{ox} > 0.8h$) oxidation, with different values for α .

Characterization

5.1 Time Resolved Photoluminescence

Time Resolved Photoluminescence (TRPL) allows for a quick and contactless optical measurement of the minority carrier lifetime in semiconductors at room temperature. Excess carriers are created by a short laser pulse and the decay of the excess minority carrier density measured over time. This decay transient delivers a so called photoluminescence lifetime, which is usually smaller than the actual lifetime. From that, the true minority carrier lifetime can be calculated by means of the diffusion equation [1]. TRPL is non destructive, very time efficient and the output data is rather easy to analyse and evaluate, especially when the transient decay shows non exponential behaviour.

There are several other optical carrier lifetime measurement methods, such as Photoconductance Decay (PCD) and Voltage Decay as well as electrical measurement methods, like Diode Current-Voltage or Pulsed MOS Capacitor Recombination, which usually require more complicated set ups or the fabrication of whole devices, thus making measurement and analysis of carrier lifetime a laborious task.

A broad overview of optical and electrical lifetime measurement techniques is given in chapter 7 of [58]. Additionally, different techniques can deliver various values for the lifetime, since they are sensitive to different mechanisms and experimental conditions do not necessarily need to be the same for every technique. A comparison of different optical methods of lifetime measurement for 4H-SiC is given in [34].

5.1.1 Experimental Technique

The intensity of the signal obtained from a TRPL measurement is of the form

$$I(t) = I_0 e^{-\frac{t}{\tau_{meas}}} \quad (5.1)$$

The measured carrier lifetime τ_{meas} is the result of several competing recombination processes. Overall, the measured lifetime is the sum of trap related recombination (SRH) τ_{srh} , radiative recombination τ_{rad} , Auger recombination τ_{aug} and surface recombination τ_{surf} [34]

$$\frac{1}{\tau_{meas}} = \frac{1}{\tau_{srh}} + \frac{1}{\tau_{rad}} + \frac{1}{\tau_{aug}} + \frac{1}{\tau_{surf}}. \quad (5.2)$$

Due to the indirect band gap of SiC, the radiative lifetime of the band-band recombination is quite long and faster processes like the capturing of carriers in a defect dominate the PL-decay. The PL-lifetime can be biased towards higher lifetimes by two step recombination effects, where the carrier first gets trapped in a defect before recombining in the band via thermal emission, but this is usually not the case at room temperature.

The injection level is the amount of majority carriers created by the excitation pulse and carrier lifetime is generally dependent on it. Usually only the high and low injection level regions are considered.

At high injection levels, the electron and hole concentrations are the same within reasonable limits, hence they decay at the same rate until they have reached the carrier concentration values at equilibrium. Until this happens their lifetimes are fixed at the high level limit τ_{hl} .

Under low injection conditions, the injected majority carriers can be treated as a mere perturbation and the lifetime is controlled by the minority carriers. TRPL measurement under low injection condition then delivers the minority carrier lifetime τ_{mcl} .

According to the SRH model (see section 2.4.7) the carrier lifetime between these two limits increases monotonically with increasing injection level, when thermal emission is neglected (room temperature). It is important to note that this model is only valid under certain (optimum) conditions and that an analytical solution for the general case has yet to be found [48]. Since in this work just the minority carrier lifetime, in this case holes, is of importance, only the low injection condition was used for the TRPL measurements.

Auger recombination becomes dominant at high injection levels above 10^{18}cm^{-3} . The injection level used in this work is well below this value and in the order of 10^{15} to 10^{16}cm^{-3} , therefore Auger recombination can be neglected. As a result, SRH and surface recombination are the processes dominating the measured lifetime

The SRH-contribution to the measured minority lifetime is given by [1]

$$\frac{1}{\tau_{srh}} = \frac{\sigma_p \sigma_n v_{th} N_T [pn - n_i^2]}{\sigma_n [n + n_i \exp(E_t - \frac{E_G}{kT})] + \sigma_p [p + n_i \exp(E_G - \frac{E_t}{kT})]} \quad (5.3)$$

where σ_n and σ_p are the electron and hole capture cross sections, respectively. N_T is the density of deep level traps, E_t the position of the trap in the band gap and v_{th} is the thermal velocity of the minority carrier $v_{th} = \sqrt{\frac{3kT}{m_h}}$. For a trap near the centre of the band gap, the equation simplifies to ($E_t \approx E_G$ and $\sigma_n = \sigma_p$)

$$\frac{1}{\tau_{srh}} = \sigma v_{th} N_T. \quad (5.4)$$

For several recombination centres the overall SRH-lifetime is simply the sum over all partial lifetimes for each trap.

The contribution of the surface recombination is somewhat similar to SRH recombination, with the exception of the two dimensional carrier trap density. The effect decreases with increasing thickness of the epilayer. The approximation equation reported [34] to be in good agreement with the exact solution [62] is a combination of the surface recombination lifetimes for the two limiting cases of the surface recombination velocity,

$$\tau_s(s_r \rightarrow 0) = \frac{d}{2s_r} \quad \text{and} \quad \tau_s(s_r \rightarrow \infty) = \frac{d^2}{\pi^2 D} \quad (5.5)$$

with the further approximation that the surface recombination velocity is the same for both surfaces (interfaces), this leads to [34]

$$\frac{1}{\tau_s} = \left(\frac{d}{2s_r} + \frac{d^2}{\pi^2 D} \right)^{-1} \quad (5.6)$$

5.1.2 Set Up

The TRPL system used in this work consisted of a frequency tripled Neodyn YLF laser emitting light at 1053nm. Non-linear optics split the beam in primary, secondary and tertiary beams of which the primary and secondary beams are filtered out. A set of mirrors filter the remaining part of the secondary beam, leaving mainly the tertiary beam with a desired wavelength of 355nm. The frequencies used for mapping and photon counting were 10kHz and 40kHz, respectively.

A lens focuses the beam, which then hits the sample under the Brewster angle $\phi_B = \arctan \frac{n_2}{n_1}$. The spot size on the sample was in the order of $85 \times 250 \mu m$. With a laser power of $0.2 mW$ the resulting injection level is $1 \times 10^{16} cm^{-3}$. The light emitted from the sample is captured by a microscope lens and focused to form a parallel beam before

entering the photomultiplier tube (PMT) with the maximum of the peak sensitivity at $400 - 500\text{nm}$. In the PMT are two filters, a long pass filter, which blocks wavelengths below 360nm , and a band pass filter at $390 \pm 10\text{nm}$ HWFM. The amplified signal from the PMT is fed to a digital oscilloscope, which averages 4000 to 30000 measurements to one curve. The sample is fixed on a computer-controlled 2-axis sliding table.

5.1.3 Temperature Dependent TRPL

In this work temperature dependent TRPL is used to determine whether an increase in lifetime is due to trapping effects, where the carriers are captured by a trap level before they ultimately recombine or due to lifetime increase via thermal oxidation.

The variation of the lifetime is observed during a temperature scan. A wavelength spectrum and lifetime transients at interesting peaks in the spectrum are obtained at every temperature step and from this it can be deduced what effects determine the lifetime.

The equipment used is mainly the same as described in section 5.1.2 with the addition of a Jabin-Jvon monochromator (HR460S) installed after the microscope lens. The monochromator consists of a single grating with 1200 lines/mm, a blaze at around 330nm and a Czerny-Turner geometry between mirror and monochromator. The focal length is 460mm .

Krishnan et al. [39] have discussed the origins and properties of various peaks in a TRPL wavelength spectra under various temperatures. They describe a reverse correlation between the band edge emission peak at 390nm and a "red" band at 670nm and a direct correlation between the band edge and the free electron concentration.

5.1.4 Injection Level Dependent TRPL

The minority carrier lifetime increases with the injection level and especially the intermediate section between high- and low injection regimes shows a strong dependence on the injection level. Injection level dependent TRPL in combination with theoretical models is used to identify the nature and capture/emission processes of complex defects such as $Z_{1/2}$.

5.2 Deep Level Transient Spectroscopy

Deep Level Transient Spectroscopy (DLTS) as developed by Lang [40] is a common way to measure properties of deep level defects. The low density and position close to the centre of the band gap of deep level traps, such as $Z_{1/2}$ and $EH_{5/6}$, make it quite hard and laborious to detect these non-radiative traps by means of photoluminescence. Additionally DLTS provides information about the activation energy, concentration

and thermal emission rate of the traps and is able to distinguish between minority- and majority-carrier traps [40].

A bias pulse is used to introduce excess carriers and the capacitance transient observed as the system returns to the thermal equilibrium after the initial non-equilibrium condition created by the pulse. The output of DLTS measurements is a plot of DLTS signal (difference of capacitance between two given times) versus temperature, where each peak in the plot corresponds to a trap, shown in fig.5.1. The height of the peak is proportional to the trap concentration and the sign indicates whether the trap captures minority or majority carriers.

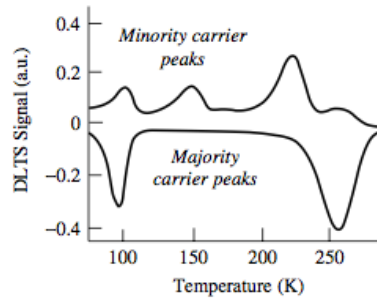


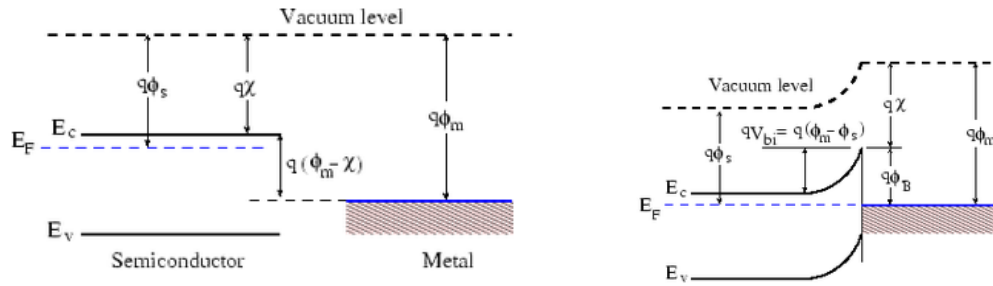
Figure 5.1: Typical DLTS Plot with majority and minority carrier traps. The height of the peaks corresponds to the trap concentration [16].

5.2.1 Contacting

Schottky contacts are used to introduce carriers and create a depletion layer in which the capture and emission process of minority carriers (in this case holes) is observed. A Schottky contact is a metal-semiconductor junction with a large barrier height, which acts as a diode (p-n junction). When current is applied to the contact a depletion layer is formed which is largely in the region of the semiconductor, since the stronger electric field in the metal prevents a depletion layer from being formed in the metal.

The work function ϕ is defined as the energy difference between the Fermi level and the Vacuum level, or in other words, the energy needed to remove a carrier from the solid. The work function for metals used in Schottky contacting ϕ_M is greater than the work function for semiconductors ϕ_S , as shown in Fig.5.2(a).

Before contacting, the Fermi level E_F of the metal and the semiconductor have different values. E_F for the metal is somewhere in the conduction band, whereas E_F for the semiconductor is in the band gap. When joining metal and semiconductor, the Fermi levels align (given thermal equilibrium) while the work functions stay the same, thus forming a Schottky barrier at the junction, shown in fig.5.2(b) for an n-type semiconductor. According to the Schottky model, assuming ideal contacting without



(a) Fermi energies and work functions of the metal and the semiconductor before contacting [4]. (b) After contacting the Fermi levels align and a Schottky barrier forms [4].

Figure 5.2: Formation of a Schottky contact and the energy levels involved.

any interface states between the metal and the semiconductor, the barrier height at the junction is determined by ϕ_M and the electron affinity χ of the semiconductor, which is the difference between the bottom of the conduction band and the vacuum level, and is given by [58]

$$\phi_{Bn} = \phi_m - \chi. \quad (5.7)$$

By this definition, the Schottky barrier height is independent of the doping concentration of the semiconductor and it should therefore be possible to adjust the barrier height by using different metals with different work functions. In experiments, however, the barrier height often proves to be independent of the metal's work function. This can be attributed to Fermi level pinning, where the Fermi level is pinned to some energy in the band gap. The exact process is not fully understood, but it was suggested [6] that surface states play an important role in the level of the barrier height, but disagreement amongst the various models is still present [64], [10], [42].

For this work, contacting was achieved by evaporating nickel ($\phi_M = 5.10\text{eV}$ [4]) on the sample under a pressure of $\approx 10^{-7}$ bar to a thickness of 1000\AA . The mask used for the evaporation allowed to make circular contacts with a diameter in the range from $0.3 - 1.2\text{mm}$. To obtain a higher capacitance and therefore less noise in the DLTS measurement, only 0.8mm and 1.2mm contacts were used for the characterization. As an ohmic contact for the backside of the sample, silver paint was used and the contacts bonded to a conduction plate.

5.2.2 Experimental Technique

There are two states a trap can assume. It can either be occupied by an electron and be in the n_T state, or occupied by a hole, it is then in the p_T state. The density of the traps in either of these two states must therefore be equal to the total density of

traps N_T

$$n_T + p_T = N_T \quad (5.8)$$

For every recombination event that occurs in the trap, the electron density in the conduction band n and the hole density in the valence band p change and are hence a function of time. The same applies to the charge states n_T and p_T . There rate with which the electron density in the conduction band changes is therefore governed by the competition of the electron emission $e_n n_T$ and capture $c_n n p_T$ process, where the capture coefficient c_n is defined by $c_n = \sigma_n v_t h$

$$\frac{dn}{dt} = e_n n_T - c_n n p_T. \quad (5.9)$$

Of course the same holds true for the steady state hole density in the valence band

$$\frac{dp}{dt} = e_p p_T - c_p p n_T. \quad (5.10)$$

From this, the change of the occupation density for the electron-occupied state is given by

$$\frac{dn_T}{dt} = \frac{dp}{dt} - \frac{dn}{dt} = (c_n + e_p)(N_T - n_T) - (c_p p + e_n)n_T. \quad (5.11)$$

This non-linear equation can be simplified because in the neutral region outside of the depletion layer, n and p are constant. Solving eq.5.11 for the steady state $t \rightarrow \infty$ under this simplification gives [58]

$$n_T = \frac{e_p + c_n n}{e_n + c_n n + e_p + c_p p} N_T. \quad (5.12)$$

Usually the emission and capture rates are not know and so additional simplifications related to the experimental conditions need to be introduced. Since the defects investigated in this work, $Z_{1/2}$ and $EH_{5/6}$, are majority traps, only this case will be considered. A schematic overview of the carrier capture and emission process during a DLTS measurement is given in fig.5.3.

In the quiescent zero bias state, the traps are filled with electrons (black circles). In the moment the reverse bias pulse is applied, the width of the depletion layer W increases and electrons are ejected from the depletion layer. In this state the capacitance has its lowest value. The emission of electrons happens faster than the usual capture process, emission is therefore dominant. In this initial emission stage the time dependency of the electron occupation n_T for a trap in the upper part of the band gap (where $e_n \gg e_p$, meaning that the defect is more likely to emit an electron rather than a hole) is given by

$$n_T(t) = n_T(0)e^{-\frac{t}{\tau_e}} \approx N_T e^{-\frac{t}{\tau_e}}, \quad (5.13)$$

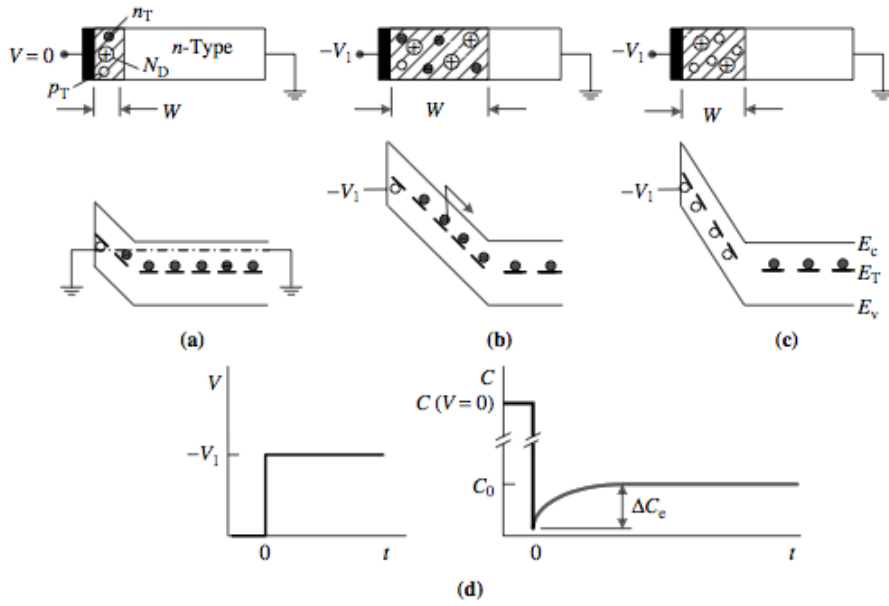


Figure 5.3: Pulse sequence during a DLTS measurement. From zero bias with capturing dominating a reverse bias is applied and emission becomes dominant. After the pulse the system returns to the steady state resulting in a transient [58].

where $\tau_e = 1/e_n$ is the emission time constant or, in other words, the lifetime of the electron in the trap. Following the initial emission of electrons eq.5.13, W decreases again and the traps relax back to the p_T state. Since the electric field pushes the electrons out of the depletion layer, a capturing process is not possible and the occupation density is determined by the thermal emission rate. In a n-type semiconductor, as considered in this work, p can be neglected to first order. The electron occupation in the quiescent reverse bias state is then given by

$$n_T = \frac{e_p}{e_n + e_p} N_T. \quad (5.14)$$

After the emission of electrons, holes will be emitted leaving electrons in the traps. This cycle results in a leaking current of the reverse biased Schottky contact as observed in I-V plots. To investigate the deep level impurities, time-varying capacitance of the Schottky contact is monitored. The capacitance during the transient phase is given by

$$C(t) = C_0 \sqrt{1 - \frac{n_T(t)}{N_D}}, \quad (5.15)$$

where C_0 is the capacitance without the presence of deep level impurities at reverse bias and N_D the doping concentration determined by a prior C-V measurement (see section 5.3) Inserting eq.?? in eq.5.15 gives the equation for the capacitance transient as shown in fig.5.3(d)

$$C(t) = C_0 \left[1 - \frac{n_T(0)}{2N_D} e^{-\frac{t}{\tau_e}} \right]. \quad (5.16)$$

As mentioned above, e_n and therefore τ_n may not be know. It is possible to calculate τ_n under the assumption that the emission and capture rates remain equal to their equilibrium values under non equilibrium conditions [58]. This gives the following expression for the emission time constant for electrons

$$\tau_e = \frac{e^{\frac{E_C - E_T}{kT}}}{\sigma_n v_{th} n_C}. \quad (5.17)$$

Fig.5.4(a) shows the temperature dependence of the time constant. It decreases with increasing temperature. Fig.5.4 shows the concept of the rate window, which is a crucial feature of DLTS. The capacitance transient is constantly obtained with a capacitance meter by scanning a temperature range while the sample is pulsed between zero and reverse bias. In this work, these transients were acquired using a National Instruments DAQ card. Digitally, a double boxcar instrument (or a lock-in amplifier) is simulated to analyze the data.

The output is the difference between the two values of the capacitance $\delta C = C(t_1) - C(t_2)$ at the two times of the rate window. The system only reacts to transients that are within the rate window adjusted by the double boxcar as shown by the response signal in Fig.5.4(b). A peak is observed when the time constant τ_e is in the range of the rate window $t_2 - t_1$. Very fast or slow decay curves result in no signal. To reduce noise in the DLTS signal, the input signal is multiplied by a reference signal and a weighing function of the form $w(t) = \delta(t - t_1) - \delta(t - t_2)$ and then averaged to enhance the signal to noise ration for the detection of low concentration. The resulting output signal can be obtained by equation

$$\delta C = C(t_1) - C(t_2) = \frac{n_T(0)}{2N_D} C_0 \left(e^{-\frac{t_2}{\tau_e}} - e^{-\frac{t_1}{\tau_e}} \right) \quad (5.18)$$

The maximum of the emission time constant, τ_e at δC_{max} from fig.5.4(b), is obtained by differentiating eq.5.18 with respect to τ_e and setting the result to zero

$$\tau_{e,max} = \frac{t_2 - t_1}{\ln(t_2/t_1)} \quad (5.19)$$

$\tau_{e,max}$ depends just on the rate window and therefore on the t_1 and t_2 setting. For every temperature set point the rate window is varied in a way that the relation $r = t_2/t_1$

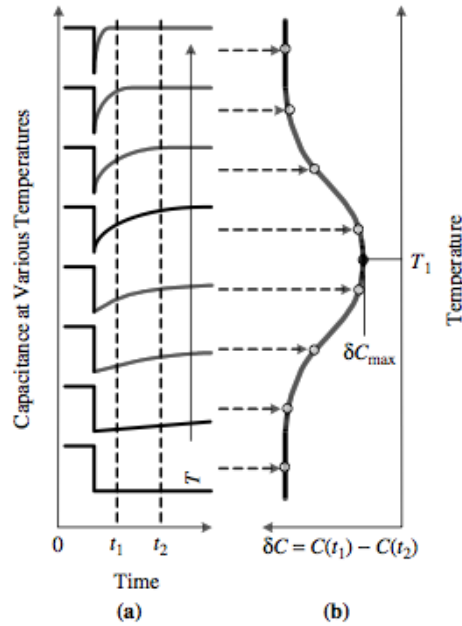


Figure 5.4: The principle of the rate window in DLTS measurements [58].

stays fixed and the values for t_1 and t_2 are varied. In this way δC for a series of rate windows is obtained to generate a DLTS plot. The trap concentration N_T can be obtained from δC_{max} from the measured $\delta C - T$ curves using the relation

$$N_T = \frac{\delta C_{max}}{C_0} \frac{2N_D e^{\frac{r}{r-1} \ln(r)}}{1-r} = \frac{\delta C_{max}}{C_0} \frac{2r^{\frac{r}{r-1}}}{1-r} N_D \quad (5.20)$$

Eq.5.19 in combination with eq.5.17 can be utilized to calculate the position of a trap level from a $\log e_n$ vs. $1000/T$ Arrhenius plot as shown in fig.5.5. From such a plot one can obtain the temperature corresponding to a trap peak at a certain rate window and calculate $\tau_{e,max}$ and from the slope E_T . The capture cross section σ is determined by the intercept of the plot with the $1000/T$ -axis.

5.3 Doping Density

The Doping density for every sample was determined by Capacitance-Voltage (C-V) measurements. The basis of this is the dependence of the depletion layer width on the reverse bias voltage. Via Schottky contacts a DC voltage is applied which creates a depletion layer of the width W depending on the voltage (and therefore on the

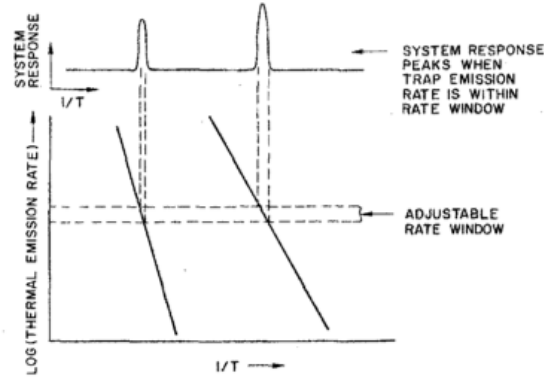


Figure 5.5: Another illustration of the rate window concept. The lower part shows a typical activation energy plot and the upper part the equivalent response of the DLTS system [58].

capacitance). The relation is given by

$$W = \frac{K_s \epsilon_0 A}{C} \quad (5.21)$$

The Schottky diode ensures that the depletion layer only extends in the semiconductor. To obtain the capacitance a small AC voltage is superimposed on the DC voltage, the best frequency and amplitude for this AC voltage depends on the approximate amount of doping and the semiconductor material.

Several simplifications are applied to calculate the doping density. For n-type semiconductors the doping density N_D is considered to be constant and no free carriers are assumed to be present in the depletion layer ($p = n = 0$). The AC voltage introduces a small charge increment dQ_m to the Schottky contact which must be balanced by an equal charge in the semiconductor dQ_s . The capacitance resulting from this is given by [58]

$$C = \frac{dQ_m}{dV} = -\frac{dQ_s}{dV}. \quad (5.22)$$

The charge in the semiconductor following said simplifications is given by

$$Q_s = -qA \int_0^w N_D dx. \quad (5.23)$$

Inserting eq.5.23 in eq.5.22 gives an expression for the capacitance depending on the change of the depletion layer width

$$C = -\frac{dQ_s}{dV} = qA \frac{d}{dV} \int_0^W N_D dx = qAN_D \frac{dW}{dV}. \quad (5.24)$$

Solving eq.5.21 for C , differentiating it with respect to V and inserting it in eq.5.24 gives an expression for the doping concentration

$$N_D = \frac{C^3}{qK_s\epsilon_0 dC/dV} = \frac{2}{qK_s\epsilon_0 A^2 d(1/C^2)/dV}. \quad (5.25)$$

It is noteworthy that to determine the doping concentration the area of the contact must be known. During a measurement $C - V$ and/or $1/C^2 - V$ curves are obtained and from the slope N_D calculated. The depth at which the doping density is evaluated can be obtained from Eq.5.21.

Simulation

A simulation can be very helpful in characterizing material properties. The simulation used to compare the experimental data with theoretical predictions in section 7.4 is based on the description of PL lifetime measurements in SiC by Klein [34, 35]. Referring to the SRH-lifetime (section 2.4.7), an excitation introduces new free holes δ_p and electrons δ_n . The time dependent density of holes and electrons can be written as

$$p(t) = p_0\delta_p(t) \quad \text{and} \quad n(t) = n_0\delta_n(t). \quad (6.1)$$

In a n-type semiconductor it can be assumed that $p_0 \approx 0$ so that the instantaneous carrier lifetime follows to

$$\tau_n(t) = \frac{1}{-\frac{(d\delta_n/dt)}{\delta_n}} \quad (6.2)$$

and the time-dependent PL intensity to

$$I_{PL}(t) = \gamma [n_0 + \delta_n(t)] \delta_p(t). \quad (6.3)$$

The decay time measured with TRPL in terms of instantaneous electron and hole lifetimes can be written as

$$\frac{1}{\tau_{PL}(t)} = \frac{1}{\tau_p(t)} + \frac{1}{\tau_n(t)} \left[\frac{\delta_n(t)}{n_0 + \delta_n(t)} \right]. \quad (6.4)$$

For low injection conditions ($\delta n \ll n_0$) this time is identical with the minority carrier lifetime τ_{MCL} . In section 3.3 it was discussed that the lifetime limiting defect $Z_{1/2}$ can assume three different charge states. The number of defects in each charge state $Z^k(t)$, $k = (+, 0, -)$ is, like the carrier concentration, time-dependent and can be

written as

$$Z^k(t) = Z_0^k + \delta Z^k(t). \quad (6.5)$$

From eq.6.1 and eq.6.5 one can see that $\delta Z^k(t)$, $\delta n(t)$ and $\delta p(t)$ are the five time-dependent variables defining the rate equations. Since the total charge is conserved and the defect concentration N_T is constant, two variables can be eliminated and the rate equations take the form:

$$\frac{d\delta n}{dt} = -(R_{n1} + R_{n2}) \quad (6.6)$$

$$\frac{d\delta p}{dt} = -(R_{p1} + R_{p2}) \quad (6.7)$$

$$\frac{d\delta Z^-}{dt} = R_{n1} - R_{p1}, \quad (6.8)$$

where the subscripts of the net capture rates R refer to the capture and emission of the respective carrier for each transition depicted in Fig.3.6. The rates follow to

$$\begin{aligned} R_{n1} &= a_{n1} \{ (n_0 + \delta n) [\delta p - \delta n - 2\delta Z^- + Z_0^0] - n_1 [Z_0^- + \delta Z^-] \} \\ R_{n2} &= a_{n2} \{ (n_0 + \delta n) [\delta n - \delta p - 2\delta Z^- + Z_0^+] \\ &\quad - n_2 [\delta p - \delta n - 2\delta Z^- + Z_0^0] \} \\ R_{p1} &= a_{p1} [(p_0 + \delta p) (Z_0^- - \delta Z^-)] - p_1 (\delta p - \delta n - 2\delta Z^- + Z_0^0) \\ R_{p2} &= a_{p2} [(p_0 + \delta p) (\delta p - \delta n - 2\delta Z^- + Z_0^0) - p_2 (\delta n - \delta p + \delta Z^- + Z_0^+)] , \end{aligned}$$

where a_{nj} and a_{pj} are electron and hole capture coefficients, respectively, depending on the capture cross section and the average carrier thermal velocity. n_j and p_j can be determined from the effective density of states for the conduction and valence band N_C and N_V with the relations [60]

$$n_j = N_C e^{-\frac{E}{kT}} \quad \text{and} \quad p_j = N_V e^{-\frac{(E_g - E_T)}{kT}}, \quad (6.9)$$

with E_T being the energy separation between the two defect levels $(-/0)$ and $(0/+)$ (see section 3.3).

From this the lifetime and PL intensity behavior over time can be simulated. It must be noted, however, that this simulation is just a rough estimation and does not account for any diffusion effects or surface recombination. More work and time is needed to further implement "real-life" effects and compare the simulation to actual TRPL measurements. Nevertheless, it offers a good way to compare theory and experiment and might give new ideas and directions for further investigations.

Experimental Series

13 samples from two differently grown wafers were divided up into 4 series, which were subjected to various oxidation temperatures and times in two different furnaces, a quartz tube furnace and an Al_2O_3 tube furnace. The goal of the experiments was to increase minority carrier lifetime in the epilayer by recombination of the carbon vacancy related deep level defect centers with carbon interstitials forming at the SiC/SiO₂ interface and diffusing into the epilayer.

One focus was set on the comparison of the defect reducing effect between oxidation in the quartz tube furnace and the Al_2O_3 tube furnace under different oxidation conditions and the increase of minority carrier lifetime, with respect to the influence of Na diffusing from the Al_2O_3 tube on the oxidation mechanism. Another one was set on the oxidation at high temperatures. Furthermore, the results were compared to samples oxidized prior to this work, in an attempt to explain their anomalous lifetime behavior at 1400°C. An overview of the oxidation conditions for every sample is given in Table 7.1

The samples used in the experiments were cut out from two different 4H-SiC wafers. The epilayers of both wafers were grown 8° off-axis towards [11-20] on [0001] Si-face n⁺ 4H-SiC substrates in a CVD reactor under a pressure of 100mbar at a temperature of 1580°C to a thickness of 42μm (x511) and 25μm (x514).

Figures 7.1 and 7.1 show the lifetime mapping of the samples used in this work prior to the thermal oxidation. As can be seen from these figures, the as-grown lifetime varies from sample to sample and also within the sample as a result of the imperfect growth. An overview of the samples used for the oxidations, their as-grown lifetime, $Z_{1/2}$ and doping concentration before the oxidation as well as oxidation conditions is given in Table 7.2.

Sample	Furnace type	T_{ox} [$^{\circ}C$]	t_{ox} [min]
Series 1			
X514-7	Quartz	1200	300
X514-D	Quartz	1200	600
X514-5	Quartz	1200	1000
Series 2			
X511-1	Al_2O_3	1300	300
X511-2	Al_2O_3	1300	600
X511-9	Al_2O_3	1300	1000
X511-6	Al_2O_3	1300	3000
Series 3			
X511-5	Al_2O_3	1400	300
X511-7	Al_2O_3	1400	600
X511-8	Al_2O_3	1400	1000
Series 4			
X511-13	Al_2O_3	1500	300
X511-15	Al_2O_3	1500	600
X511-12	Al_2O_3	1500	1000
Reference Series 1			
X460-7	Al_2O_3	1150	300
X460-8	Al_2O_3	1150	600
x460-1	Al_2O_3	1150	900
Reference Series 2			
X460-4	Al_2O_3	1300	300
X460-13	Al_2O_3	1300	600
x460-10	Al_2O_3	1300	900
Reference Series 3			
X460-11	Al_2O_3	1400	150
X460-14	Al_2O_3	1400	300
x460-17	Al_2O_3	1400	450

Table 7.1: Label, type of furnace and oxidation temperature and time used for the samples of this work as well as the reference samples. The oxidation time given in the table excludes the heating up and cooling down times.

Sample	$\tau_{AG}[ns]$	$N_D [10^{14}mm^{-3}]$	$N_T [10^{13}mm^{-3}]$	$\sigma_n [10^{-14}cm^2]$
x514-7	140	4.78	1.42	1.70
x514-D	128	3.99	2.76	1.72
x514-5	155	5.87	3.91	1.79
x511-1	239	5.60	1.32	2.03
x511-2	215	5.07	0.42	3.95
x511-9	319	5.67	0.85	3.37
x511-6	268	4.37	0.83	2.27
x511-5	250	4.21	1.08	1.29
x511-7	230	5.16	1.20	2.31
x511-8	313	5.74	1.18	2.52
x511-13	258	5.26	3.10	2.64
x511-15	290	6.39	13.80	2.19
x511-12	290	4.89	14.4	2.35

Table 7.2: As-grown mean lifetime, doping concentration and $Z_{1/2}$ oxidation temperature T_{ox} and time t_{ox} and electron capture cross section σ_n of the samples used in the experiments

Sample	$\tau_{ox}[ns]$	τ_{rel}	$N_T [10^{13}mm^{-3}]$	$\sigma_T[10^{-14}cm^2]$	$d_{ox}[\mu m]$
x514-7	159	1.14	14.5	2.81	0.33
x514-D	183	1.43	2.76	—	0.35
x514-5	280	1.81	3.91	—	0.66
x511-1	563	2.36	—	—	0.29
x511-2	674	3.13	0.27	0.40	0.39
x511-9	848	2.66	—	—	0.55
x511-6	893	3.33	3.85	0.73	1.02
x511-5	1000	4.00	2.69	1.15	0.74
x511-7	1132	4.92	3.82	0.92	0.96
x511-8	1172	4.04	3.02	0.55	0.99
x511-13	1175	4.55	1.91	1.36	1.01
x511-15	1411	4.87	1.97	0.65	1.23
x511-12	1562	5.39	—	—	1.40

Table 7.3: Lifetime of oxidized samples τ_{ox} , relative lifetime increase τ_{rel} , density and electron capture cross section of the new defect N_T and σ_T and oxide thickness d_{ox} .

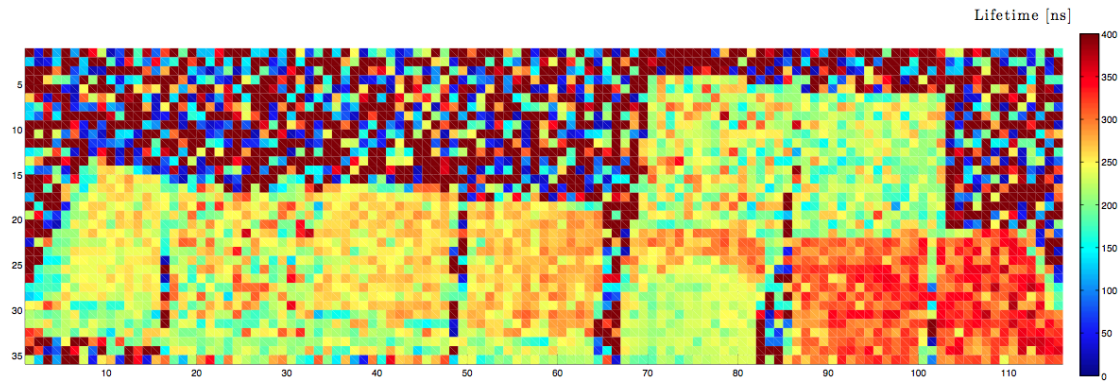


Figure 7.1: TRPL lifetime mapping of the as-grown x511 samples. Each data point represents the fitted lifetime value from a lifetime transient measurement at this point at room temperature. The samples in the first row are from left to right x511-1, x511-2 and in the second row x511-3, x511-4, x511-5, x511-6, x511-7, x511-8, x511-9.

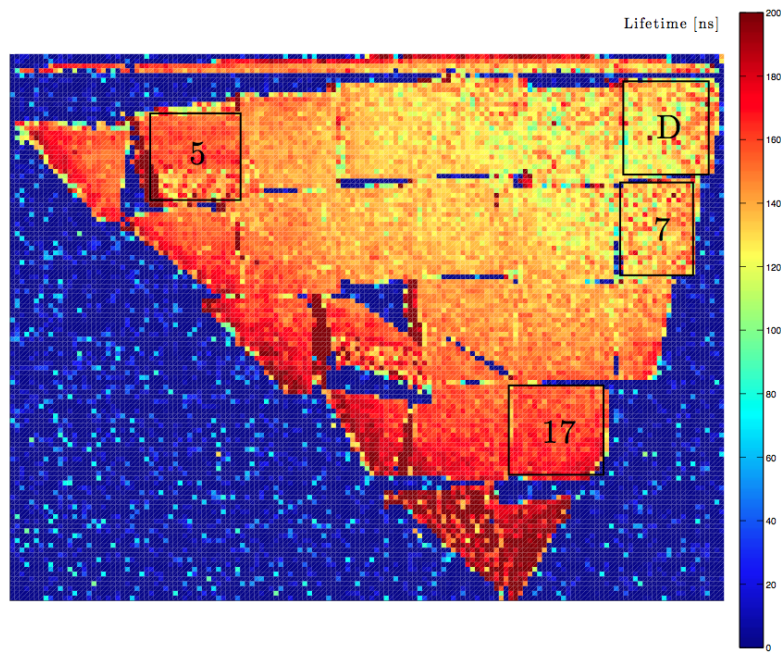


Figure 7.2: TRPL lifetime mapping of the as-grown x514 samples. Each data point represents the fitted lifetime value from a lifetime transient measurement at this point at room temperature. The samples used in this work are indicated.

7.1 Experimental Details

The procedure of sample preparation, DLTS and TRPL measurements before and after the oxidation was the same for every sample and is depicted in Fig.7.3 and described below.

Before the evaporation of the Ni contacts onto the samples, every sample underwent thorough cleaning according to the standard Radio Cooperation of America (RCA) cleaning procedure. First, dirt on the sample was removed by dipping it in boiling acetone and ethanol for at least 3 minutes and scrubbing it with a q-tip (C1). Next, organic contamination was removed by a dip in H_2O , NH_3 and H_2O_2 (RCA1) with a 5:1:1 ratio at 85°C for 5 minutes (C2). Inorganic contamination was removed by another 5 minute dip in H_2O , HCl and H_2O_2 (RCA2) with a 6:1:1 ratio at 85°C (C3). Finally the oxide present on the samples was removed by a dip in HF acid for 1 minute at room temperature (C4).

Contacting was done by evaporating Ni in a Moorfield Minilab VP60M thermal evaporator at a pressure of 10^{-7} to 10^{-5} bar through a mask, which creates circular contacts with diameters of 0.8 and 1.2mm. The evaporation was stopped automatically after a deposition thickness of 100nm measured by a quartz crystal.

Following the evaporation, the samples were fixed on a contact plate with silver paint, which also acts as an ohmic contact for the substrate side of the sample, and the contacts of the sample and the plate bonded together with an Al wire.

Before DLTS measurement, I-V and C-V curves were obtained for every sample, to determine diode characteristics (I-V) and doping concentration (C-V see section 5.3). The DLTS spectra were measured for three contacts on every sample in a temperature range from 220 to 650K in 2K steps, with a filling pulse width of 10ms. Rate window adjustments have been performed and the average deep level defect concentration determined, according to section 5.2.

Several test measurements have shown that a TRPL measurement after superficial removal of the Ni contacts results in a very low to no PL signal from the sample. Hence the measurement sequence, where TRPL is performed before DLTS prior to the oxidation. It is, however, unavoidable to measure the lifetime again following DLTS after thermal oxidation. Additionally, the oxidation process is greatly disturbed when contacts are present on the sample. Therefore, prior to the oxidations, the samples were cleaned (C1, C2, C3) and the contacts removed with a 15 minutes dip at 85°C in HCl and H_2O_2 with a 1:1 ratio. Although no visible residue of the contacts remained after the dip, the PL signal was still disturbed, probably by the presence of Ni atoms in the surface region due to diffusion during the DLTS measurements. To remove the remaining influence of the Ni contacts due to diffusion or nickel silicide formation during the DLTS measurement, the first 50nm of the epilayer have been removed by ICP etching under an N and O_2 atmosphere for 5 minutes. This treatment resulted in

a satisfactory result during the TRPL measurement and no influence on the oxidation was evident. After another HF dip (C4), the samples were oxidized.

After the thermal oxidation, the oxide thickness throughout the sample surface was measured by optical interferometry and the surface morphology inspected with an optical microscope under 10, 50, 200, 400 and 1000 fold magnification and the use of a polarization filter to remove light scattering from the backside of the sample.

The lifetime after the oxidation was investigated by TRPL-lifetime mapping of every sample and temperature dependent TRPL at various temperatures to check for eventual trapping effects which can create seemingly higher lifetimes.

After another cleaning (C1, C2, C3, C4), Ni contacts were evaporated onto the oxidized sample and DLTS was used to determine the change in $Z_{1/2}$ concentration due to the oxidation process.

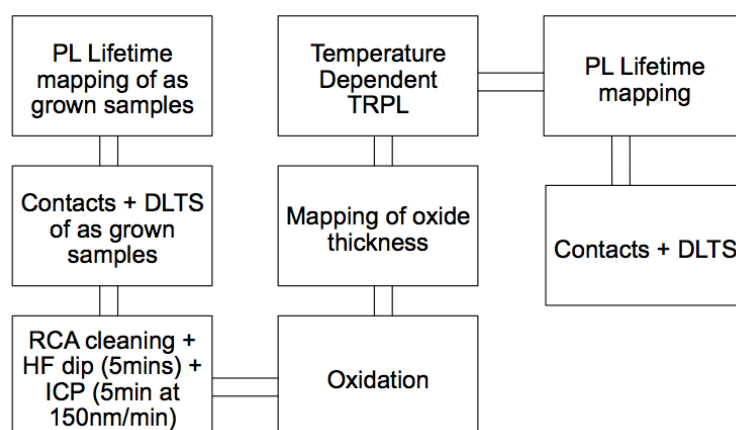


Figure 7.3: Experimental cycle of the samples.

7.2 Increase in Minority Carrier Lifetime by Thermal Oxidation

The thermal oxidation of the 4H-SiC samples produced an increase in lifetime throughout all series. The absolute and relative amount of the lifetime increase depends on oxidation time and temperature, since the recombination of interstitials with vacancies is a temperature dependent process [29]. In agreement with the literature, the lifetime increases fast initially (for oxidation times of 300 to 600 minutes) and shows a saturating behavior for longer oxidation times. The reason for this saturation may lie in the accumulation of carbon clusters at the SiC/SiO₂ interface and the resulting dependence of the oxide growth rate with the oxidation time (see 4.1). Fig.7.7 shows

the lifetime at all temperatures and times used in the experiments.

The general trend, that the saturation of the lifetime increase occurs later in terms of oxidation times with increasing oxidation temperatures, becomes apparent from the lines connecting the measured lifetimes shown in Fig. 7.7. This behavior can be explained within the Si-C emission model by a combination of the larger diffusion length of the C interstitials at higher temperatures, allowing them to recombine with C vacancies deeper in the epilayer and the higher thermal velocity of the interstitials, allowing them to penetrate through a thicker layer of interstitial built up at the interface. The lifetime increase is clearly visible in the lifetime mappings in figures 7.4, 7.5 and 7.6. It can be seen that the increase in lifetime is not constant over the sample surfaces. This is mainly due to varying surface properties as well as unpredictability of the airflow during oxidation and localized crystallisation of the oxide.

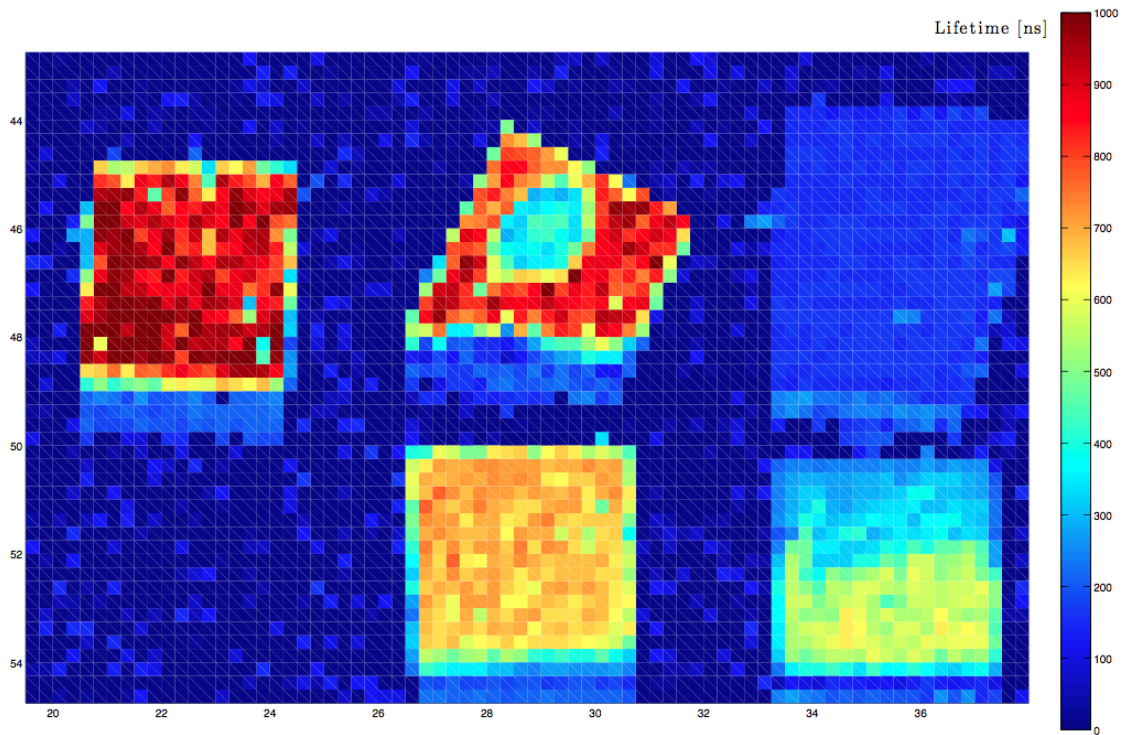


Figure 7.4: TRPL lifetime mapping of the oxidized samples. Each data point represents the fitted lifetime value from a lifetime transient measurement at this point at room temperature. The samples in the first row from left to right are x511-6, x511-9 and x514-7. The samples in the second row are x511-2 and x511-1.

The saturation behaviour mentioned above can also be seen in Fig.7.8, where the slope for every data point of the potential fit to the measured oxide thicknesses becomes

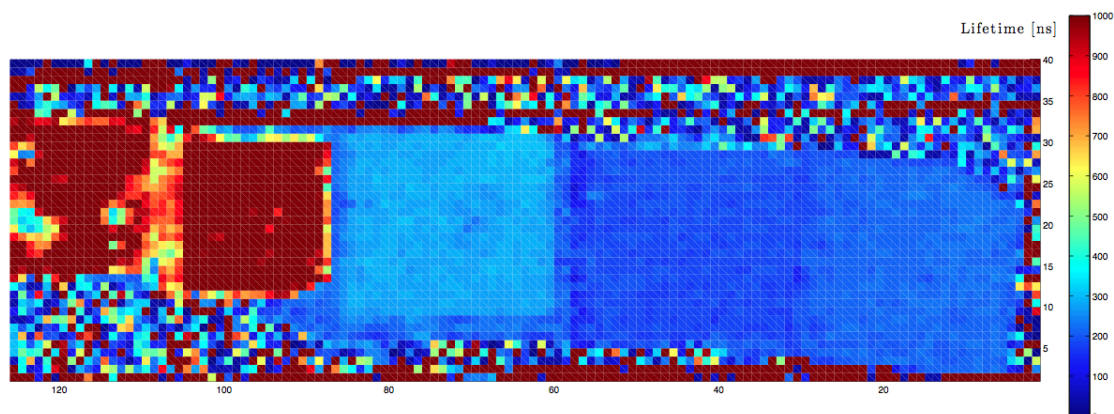


Figure 7.5: TRPL lifetime mapping of the oxidized samples. Each data point represents the fitted lifetime value from a lifetime transient measurement at this point at room temperature. The samples from left to right are x511-8, x511-7 and x514-5, x514-D and x514-7.

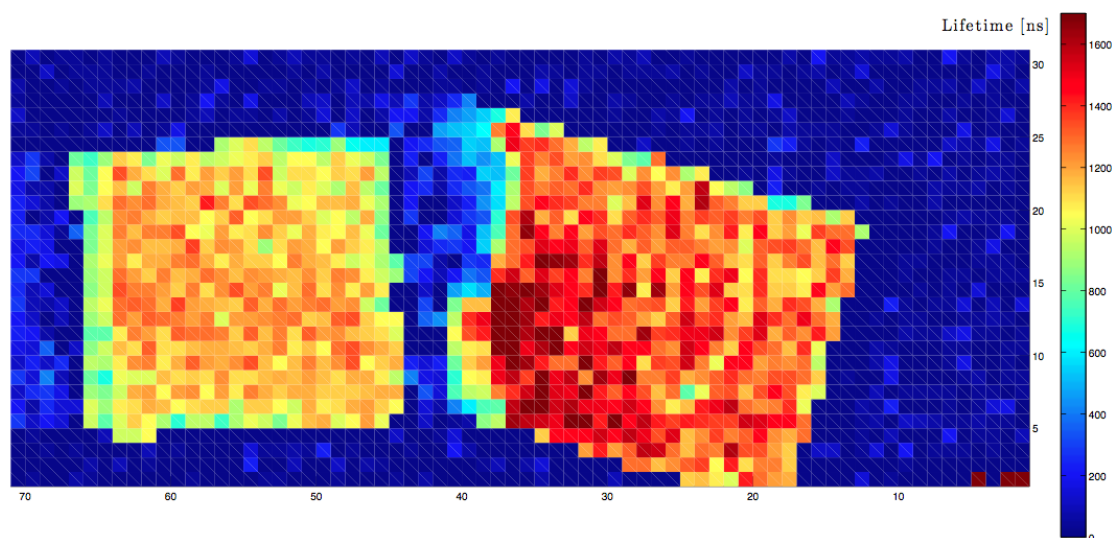


Figure 7.6: TRPL lifetime mapping of the oxidized samples. Each data point represents the fitted lifetime value from a lifetime transient measurement at this point at room temperature. The samples from left to right are x511-13, x511-15.

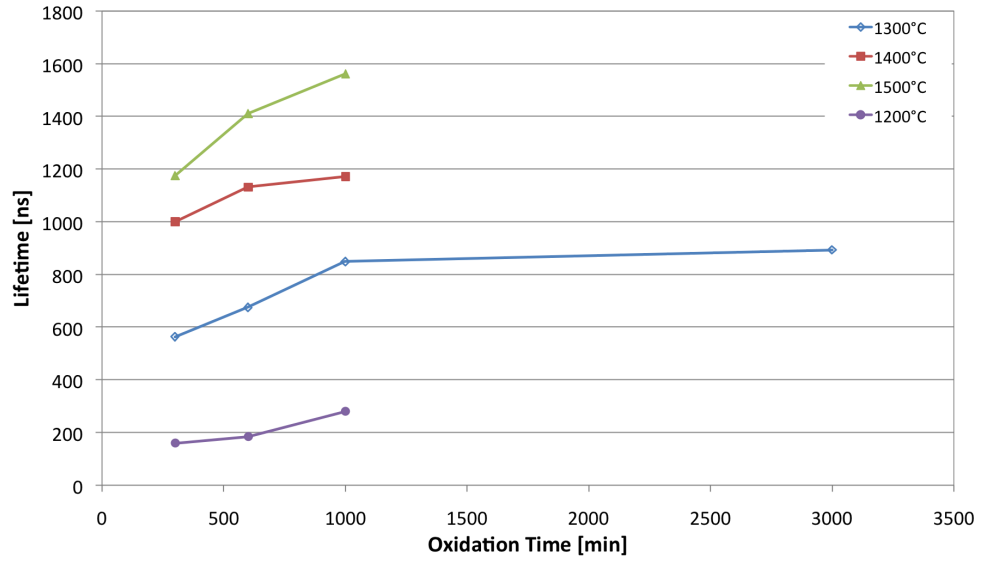


Figure 7.7: Minority carrier lifetimes after the oxidation according to Table 7.1. The markings represent the lifetime of the sample averaged over the whole sample surface. The lines connecting the markings are guides to the eyes.

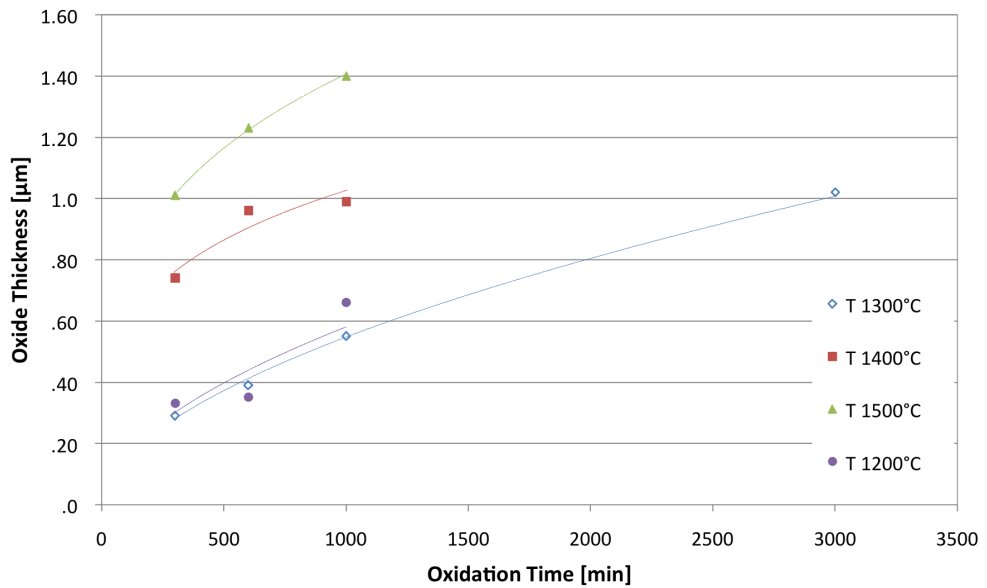


Figure 7.8: Oxide thicknesses after oxidation. The Markings represent the average thickness over the sample surface as measured by interferometry. The lines are fits by a power law of the form $y = Ax^b$. (T1200: $A=0.013$ $B=0.547$; T1300: $A=0.011$ $B=0.555$; T1400: $A=0.183$ $B=0.249$; T1500: $A=0.214$ $B=0.272$)

steeper with increasing oxidation temperature. This indicates a connection between the oxide thickness over oxidation time and the level of lifetime increase by thermal oxidation, thus making the oxide thickness and the lifetime increase proportional quantities for a specific oxidation time. It is, however, noteworthy that in Fig.7.8, contrary to Fig.7.7, the oxide thickness for the oxidation at 1200°C increases faster than for 1300°C. It can be credited to the fact that the oxidation at 1200°C was done in a quartz tube furnace under "cleaner" conditions compared to the Al_2O_3 furnace which is more exposed to the environment due to its construction. Furthermore Na diffusion from the Al_2O_3 tube and the oxygen partial pressure might have also an effect on the oxide growth. Contrary to MOS device fabrication, the quality of the oxide is only of minor importance to the lifetime increase compared to the oxidation temperature. This behavior does not affect the lifetime and doesn't change the 1200°C curve.

A comparison between the absolute and relative lifetime is shown in Fig.7.9. The relative lifetime increase shows a very large scatter with oxidation temperature and time. This is the result of a superposition of various hard to be controlled influences, such as variations in the wafer material, difficulties in reproducing the same oxidation conditions for every sample and physical processes in the sample. The saturating behavior with oxidation time appears to be only present at 1500°C. The data tentatively suggests that the initial $Z_{1/2}$ concentration (which determines the initial lifetime) has less influence on the achieved lifetime after oxidation than the oxidation conditions. The samples X460 oxidized prior to the samples in this work showed a peculiar behavior at 1400°C. The lifetime after oxidation of the X460 samples at 1400°C is up to two times bigger than the lifetimes achieved at the respective temperature in this work. The lifetimes of X460 and the samples from this work are shown in Fig.7.10. Furthermore the observed decrease and increase in lifetime over oxidation time as seen in Fig.7.10 and 7.11 does not accord with the results from this work or the results from the X460 samples oxidized at lower temperatures. Since the oxidation at 1400°C in this work did not deliver any unexpected results regarding the lifetime increase, the anomaly of the X460 samples may be related to the growth conditions, which varied from the conditions of the samples used in this work, but could not be fully explained. The relative lifetimes of the X460 samples in comparison to the series of this work are depicted in Fig.7.11. For it, the same principle is valid as mentioned for the relative lifetimes of X511 and X514.

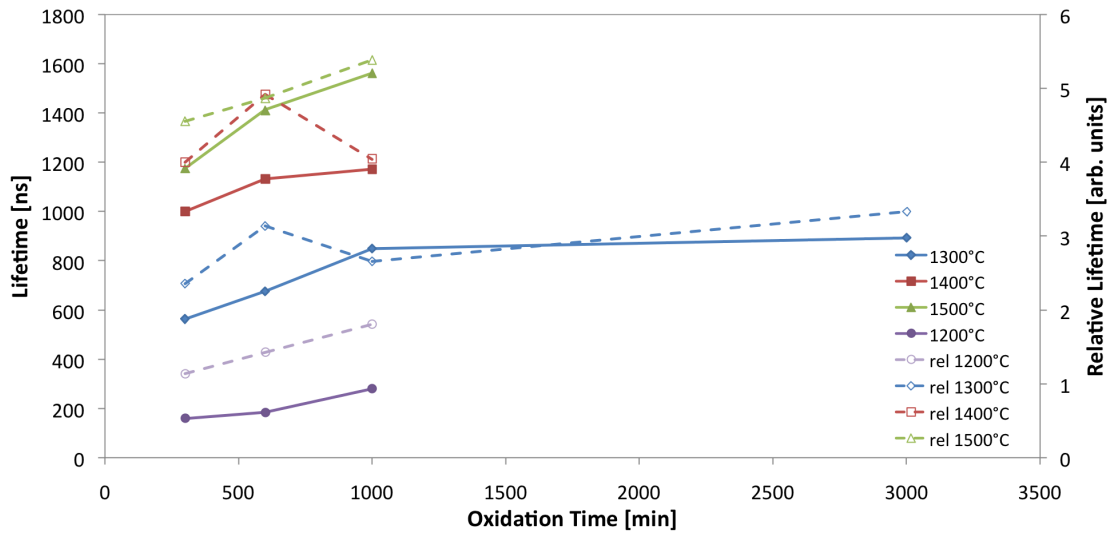


Figure 7.9: Absolute and relative lifetime after the oxidation. The lines connecting the data points are guides to the eyes. Full markings and lines represent the absolute values, while empty markings and dotted lines are relative values. The relative lifetimes was calculated simply by dividing the absolute lifetime after the oxidation by the as-grown lifetime.

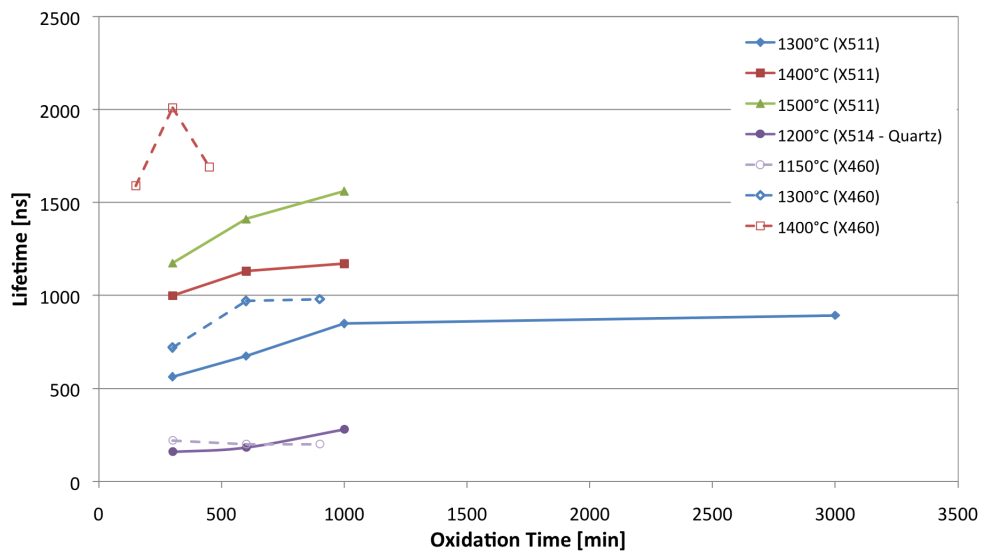


Figure 7.10: The lifetime of the reference series compared to X511 and X514. Full markings and lines represent the absolute lifetimes from this work. Empty markings and dotted lines refer to the X460 series. The peculiar behavior of X460 at 1400°C (red dotted line) remains unexplained.

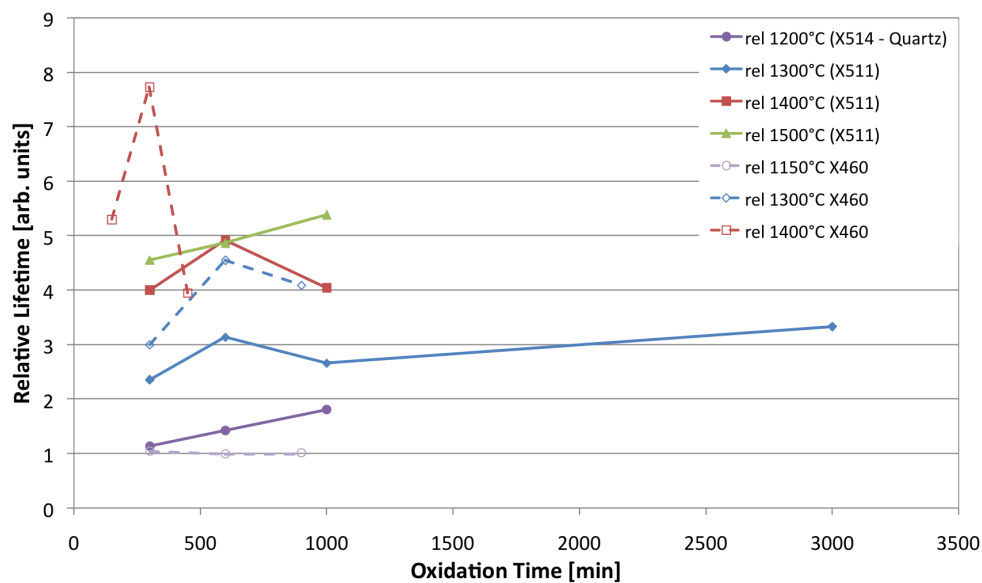


Figure 7.11: Relative lifetime increase of the X460 series. Like in Fig.7.10 the relative lifetime also shows a peculiar behavior at an oxidation temperature of 1400°C.

7.3 PL Spectra and TRPL

To investigate the various sources of photoluminescence from the samples, PL spectra were recorded at different temperatures ranging from 82K to 400K over a wavelength range from 350nm to 700nm. The main concern leading to the choice of this method, was to determine whether there are new recombination centers or mechanisms present after the oxidation, specifically near the band-edge.

The minority carrier lifetime was measured with TRPL at a wavelength of 390nm which corresponds to the energy released by free exciton recombination. This recombination mechanism is believed to be of intrinsic origin [38] and therefore a good indicator for the minority carrier lifetime. If new mechanisms or centers exist after oxidation and emit radiation at a wavelength close to 390nm, it could falsify the measured lifetime and create the impression of a much larger lifetime increase than actually expected from the thermal oxidation process.

Fig.7.12 shows a representative room temperature PL spectrum of sample X511-8 obtained before oxidation. At room temperature, the PL spectrum shows two pronounced peaks A and B centered at 390nm and 355nm, respectively. Peak B is an artifact from the excitation laser reflected from the surface of the sample and can be disregarded in this investigation. Peak A is the band edge UV emission used for lifetime measurements. The band edge peak is relatively broad at room temperature. Centered at

508nm a smaller but very broad peak C is visible, which could involve boron, titanium, and other kinds of deep levels [39]. The variations of the PL spectra amongst the samples are due to varying defect concentrations and slight changes in the alignment of the lenses since the samples couldn't be measured all in the same session

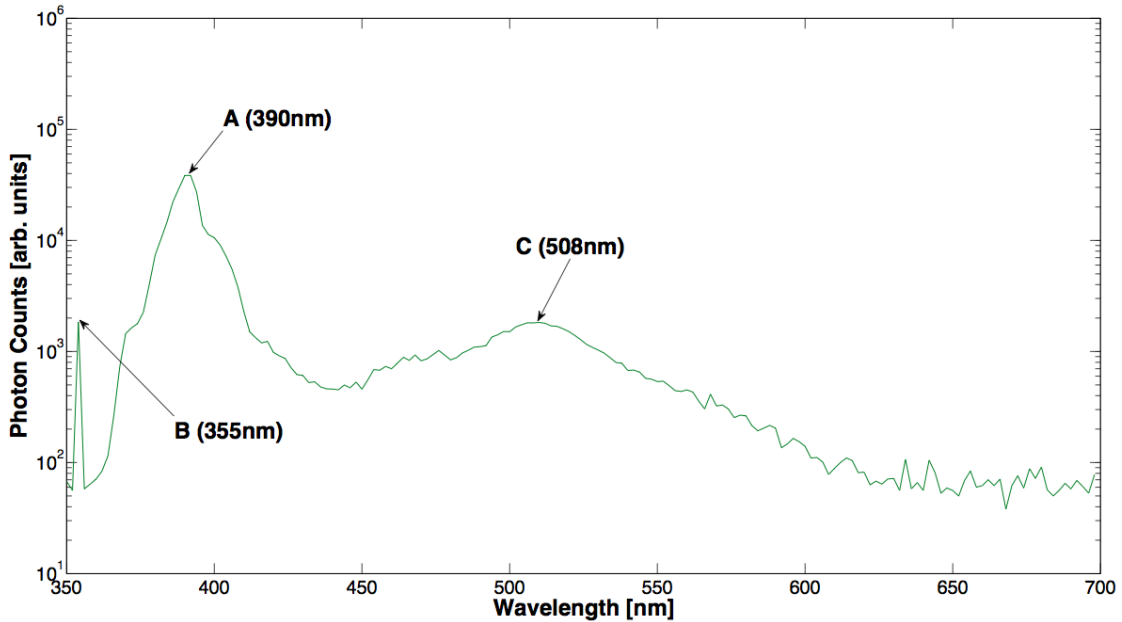


Figure 7.12: Representative room temperature PL spectrum of an unoxidized sample (X511-8). The spectrum shows three distinct peaks. Peak B is a result of laser artifacts, peak A is the band edge emission and peak C is of unknown origin and can only be speculated to be related to deep levels [39].

At lower temperatures, thermal excitation and recombination decreases and only recombination from deep levels and other defects or dopants contribute to the PL spectrum, which results in a more detailed investigation of the samples. Fig.7.13 shows the spectrum of a representative unoxidized sample with a good PL signal at various temperatures. Peaks A,B and C become sharper and new peaks appear, revealing that the broad band-edge peak actually consists of two different peaks A1 centered at 390nm and A2 centered at 402nm. The small peak centered at 428nm labeled D appears only at temperatures below 120K. A1 is the band-edge emission which was overlapped by another peak at room temperature. With lower temperature the band edge peak shifts slightly to higher energies. Peaks A2 and D follow the spectral behavior of two phonon replica. With temperature increasing from 82K to 120K, A2 and D become smaller and eventually disappear above 120K, while the band edge peak remains and broadens. The observation that the peaks corresponding to the two phonon replica and the band

edge peak both gain in luminescence with decreasing temperature suggests that their respective recombination mechanisms are not competing.

Fig.7.14 shows the TRPL spectra at various temperatures of sample X511-8 after the oxidation. The arrows on the various peaks indicate the maximum fit to the lifetimes measured at the respective wavelengths and temperatures. The lifetimes indicated at the band edge peak at 300K are in the range of the measured lifetimes from the mappings, whereas the lifetime measured at the other peaks differs from those values and shows peculiar behavior with temperature. For all peaks except the band edge peak, the lifetime decreases with increasing temperature.

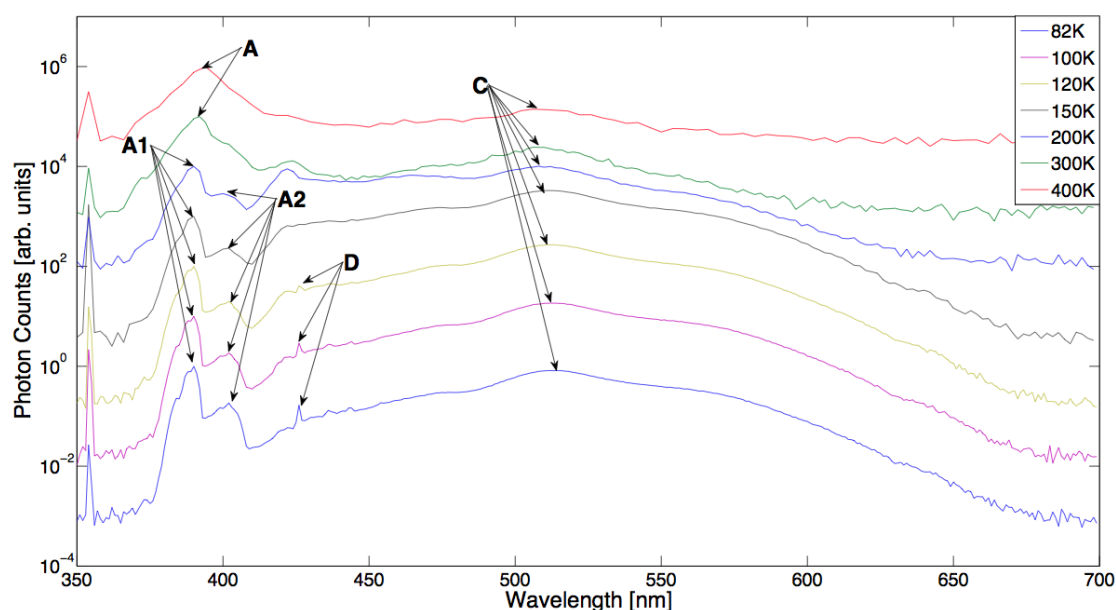


Figure 7.13: Representative PL spectra of an unoxidized sample (X511-8) at temperatures from 82K to 400K. For visual clarity, the spectra are separated by a factor of 10 each. The band edge peak separates in two peaks as the temperature decreases from room temperature and a new peak arises below 120K.

Comparing the PL spectra from the unoxidized samples in Fig.7.13 to the oxidized samples in Fig.7.14 shows that there is barely any luminescence at the wavelength assumed to be related to the two phonon replica. This leads to the assumption that the disappearance of the two phonon replica is a direct consequence from the oxidation. Furthermore, the relation between the size of the artifact peak coming from the laser and the band edge peak has changed after oxidation, with the first being larger and the latter smaller compared to before the oxidation. A possible explanation is that the surface of the sample is rougher after all the treatments the sample has undergone (see section 7.1). Less light goes in and out of the sample, resulting in more reflexion from

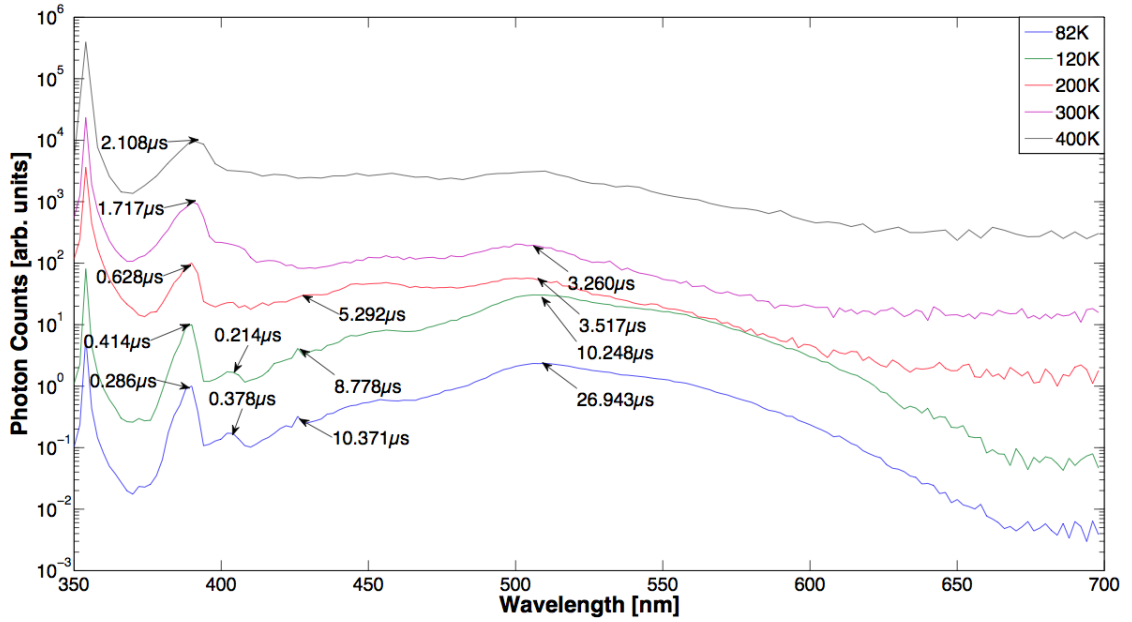
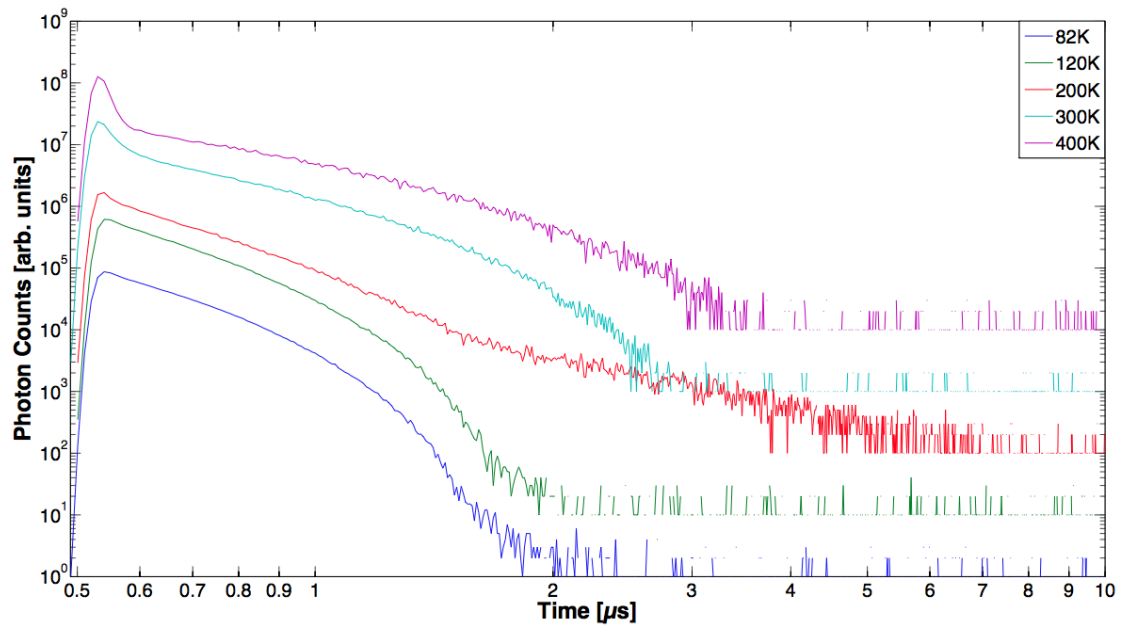


Figure 7.14: PL spectra of an oxidized sample (X511-8) at various temperatures. The oxidized sample shows fewer and smaller peaks compared to the as-grown state in Fig.7.13. The arrows indicate the maximum-fit lifetimes at the respective wavelengths and temperatures. Peaks without indication had too small signals for the lifetime to be measured reliably.

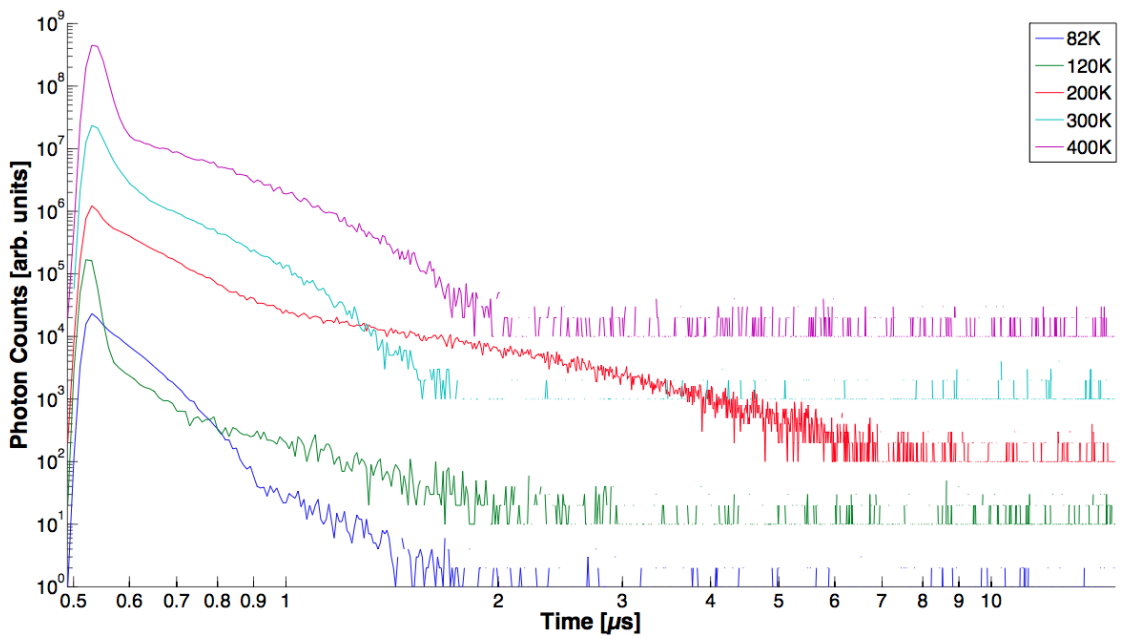
the laser and less luminescence from the sample. Of course, changes in the alignment of the experimental set up can not be disregarded.

The consideration of the lifetimes at the various peaks delivers the same result as before. The, now increased, lifetime measured at the band edge wavelength is in the range of the mapped lifetimes from Table 7.2. From that it can be assumed that the lifetime increase results from the band edge and no other band and the lifetime mappings are therefore valid measures of the free carrier lifetime. A high intensity of the band edge emission is believed to be an evidence of high purity of the material and high value of the minority carrier lifetime [39]. In accordance to this, disregarding the intensity losses at the surface of the samples, the band edge signal is dominant throughout the whole temperature range used in this work.

The analysis of the TRPL transients before oxidation revealed several peculiarities in the as grown samples, that were not expected to show and are somewhat contrary to the literature. All samples showed the same anomalous features in varying magnitudes. Fig.7.15(a) and Fig.7.15(b) show the transience of the PL signal over time of the samples X511-8 and X514-2 before oxidation, respectively. The plot is double logarithmic to make visual interpretation easier.



(a) PL transient of X511-8 in the as-grown state.



(b) PL transient of X514-2 in the as-grown state.

Figure 7.15: PL transients of unoxidized samples X511-8 and X514-2 with double logarithmic scale. Both show a sudden increase in lifetime at 200K and multi exponential behavior

Let us first consider the multi-exponential decay. From literature [1] the transience of the PL signal, influenced by SRH-recombination at a single deep level, is expected to follow a single exponential law. Analysis of the DLTS signals of the sample series X511 and X514 showed only two kinds of defects, $Z_{1/2}$ and $EH_{6/7}$. Since $EH_{6/7}$ is believed to have no effect on lifetime, the recombination path via $Z_{1/2}$ should remain as the major recombination path to influence near-band edge photon emission. Fig.7.15(a), however, shows the multi-exponential decay of the PL signal of sample X511-8, which arises at 200K and gets increasingly pronounced as temperature rises. This behavior is even more present in the samples from the X514 wafer. Fig.7.15(b) shows the transients of sample X514-2. Multi-exponential decay is present from 82K on and gets increasingly pronounced as temperature rises, like it was the case for the X511 samples.

All transients with multi-exponential decay exhibit the same behavior. After the carrier injection, the signal decays very fast for about a third of the whole decay time. Then follows the longer decay curve, the maximum fit values to these second decays are the lifetimes indicated in Fig.7.14. The fitting function used is a single exponential superimposed over a linear background.

Another feature observed in the TRPL curves of all as-grown samples is the anomalous increase of the decay time in the temperature range from 82K to 400K. This is contrary to the results published by Klein et al. [35], which suggest that the PL decay time remains constant until about 400K and rises with temperature thereafter (7.16). Kordina et al. measured an increase of the decay time from 300K to 500K in accordance with the findings of this work (Fig.7.16). It does not, however, give any information about the decay time below 300K. Additionally, throughout all series, the decay time showed an unusually high value at 200K. The corresponding thermal activation energy is in the region of 3eV. The reason for this behavior of the lifetime over temperature remains unclear and further investigation is needed, but since there were no obscurities in the DLTS spectra of the as-grown samples (Fig.7.18), this behavior might be related to hole traps. The strong dependence of the lifetime from the temperature and the multi-exponential decay suggest that the recombination via the $Z_{1/2}$ center might not be the only recombination path.

Except for the increase in lifetime with temperature, the decay curves of the oxidized samples show no irregularities. Representative PL transients are shown in Fig.7.17. The decay is single-exponential and there is no extraordinary jump in lifetime throughout all series. This may lead to the conclusion that the behavior of the as-grown samples results from defects that are annihilated during thermal oxidation.

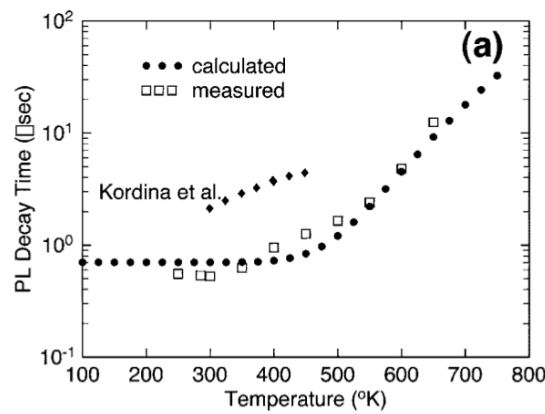


Figure 7.16: Measured temperature dependence of the PL lifetime (open squares) compared to the simulated behavior (solid circles) [35]

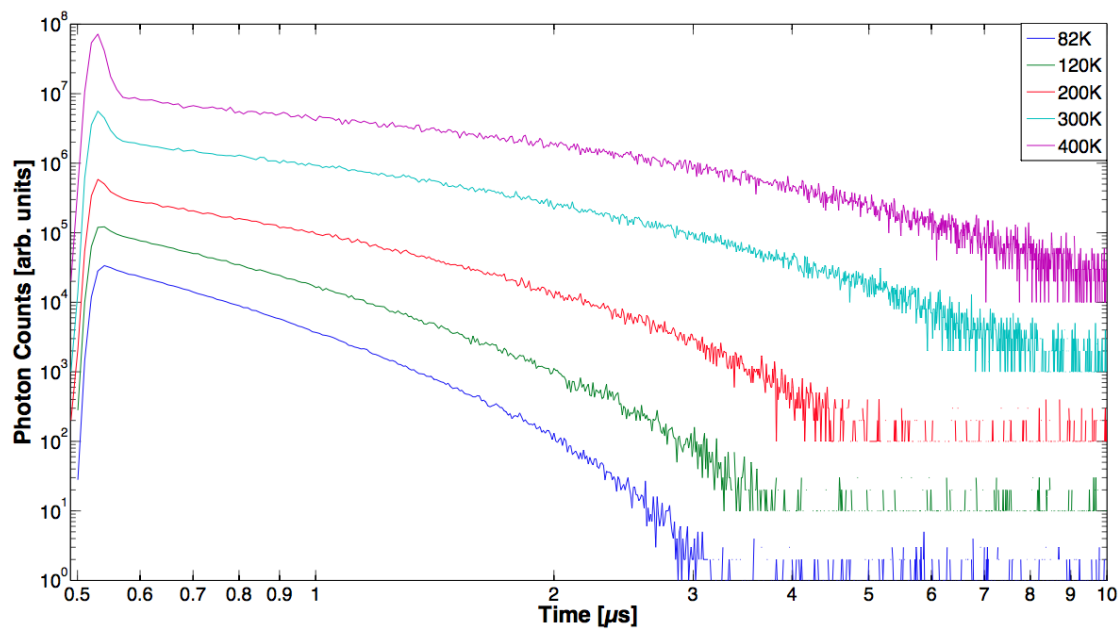


Figure 7.17: PL decay transients at various temperatures of X511-8 after oxidation. The sudden lifetime increase and multi exponential behavior have disappeared after the oxidation.

7.4 Deep Level Transient Spectroscopy

Comparing the DLTS spectra before and after oxidation shows another unexpected result. Fig.7.18 shows the DLTS plots of sample X511-13 before and after the oxidation including three rate windows each. The goal of thermal oxidation was for the C interstitials to recombine with the C vacancies thus reducing the $Z_{1/2}$ and $EH_{6/7}$ concentration. While this was observed, the $Z_{1/2}$ and $EH_{6/7}$ concentration was reduced to below the detection limit of 10^{11} cm^{-3} , two new peaks X and Y were observed. Both the reduction of $Z_{1/2}$ and $EH_{6/7}$ and the appearance of the new defects occurred in all samples in every series. To rule out erroneous measurement, some samples were measured with up to three contacts and two different configurations of the sample holder in the DLTS setup. Additionally, a variety of unoxidized reference samples from different wafers have been measured. None of them showed any obscurities. From the

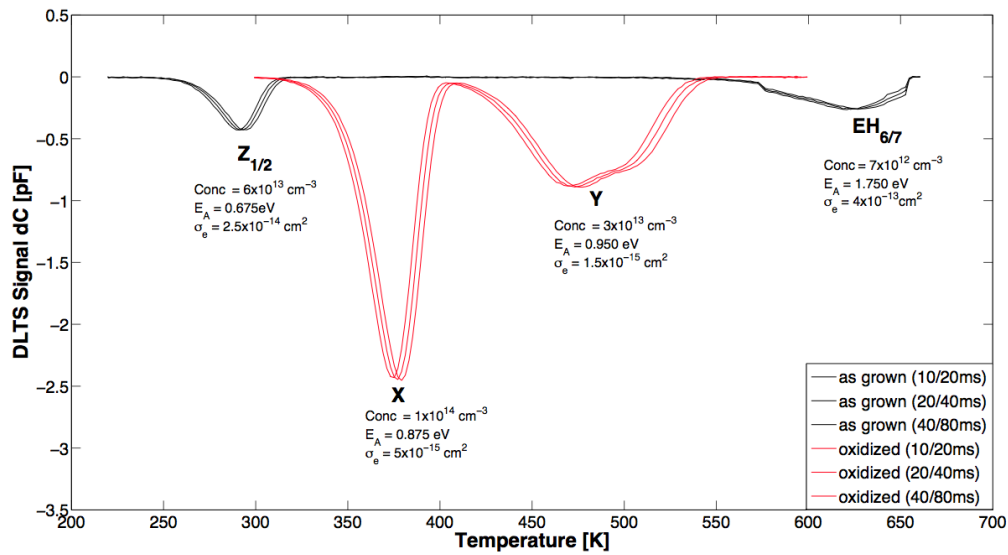


Figure 7.18: DLTS plot of X511-13 as-grown (black lines) compared to after the oxidation (red lines) with three different rate windows at the same relation. The value of the rate windows are shown in the legend, with the smallest rate window being on the high temperature side.

DLTS measurements, some basic information of the new defect X could be acquired. X shows an increased activation energy of 0.870eV compared to 0.675eV of $Z_{1/2}$. The electron capture cross section is around $5 \times 10^{-15} \text{ cm}^2$ and therefore smaller than for $Z_{1/2}$ by an order of magnitude (The more important hole capture cross section could not be determined due to shortcomings of the DLTS equipment). The concentration of X, shown in Fig.7.19 over the oxidation time for various temperatures, varies from sample to sample but shows the trend to increase with oxidation time and temperature.

It is noteworthy that the initial $Z_{1/2}$ concentration has no effect on the concentration of X after the oxidation.

First considerations regarding the nature and properties of these new defects suggested that they might be related to extended defects.

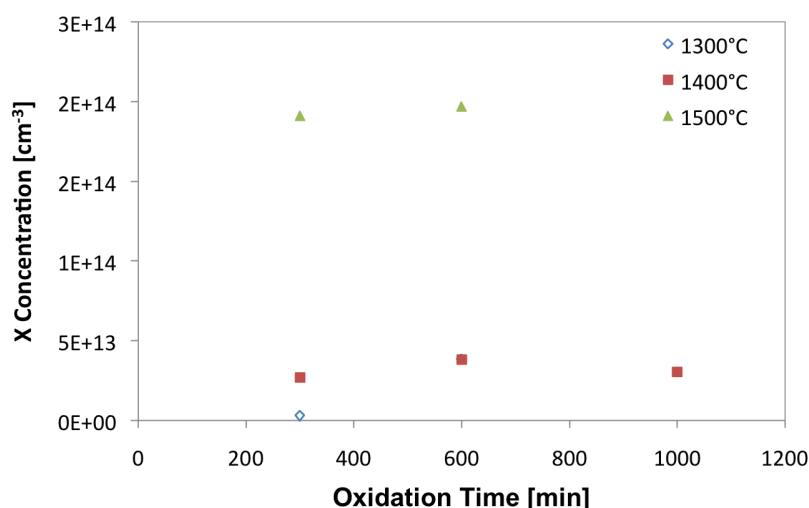


Figure 7.19: Concentration of the new defect X over oxidation time for three oxidation temperatures. Missing data points could not be acquired due to heavy noise in the DLTS signal of some samples.

Unlike point defects, extended defects, such as dislocations, grain boundaries, precipitates form closely spaced electronic states. Surface and interface states are generally point defects but they might also form a network of extended defects at the surface during oxidation. Extended defects can be identified and distinguished from point defects with DLTS by variation of the filling pulse width. In a DLTS temperature spectrum, extended defects are primarily noticeable by a symmetric or asymmetric peak broadening with longer filling pulses, compared to the symmetric narrow peaks coming from point defects. It is because extended defects are many-electron defects, that their electronic structure in the band gap is shaped like an electronic band, rather than a single energy state as formed by point defects. Therefore, longer filling pulses mean more electronic states at the extended defects get filled with carriers. The resulting peaks become broader and greater in amplitude until the filling pulse is long enough to completely fill all electronic states of the traps with carriers, at which point the shape of the peak does not change anymore. The single energy states at point defects, however, are filled after relatively short pulse lengths, meaning that the corresponding DLTS peak will not change with filling pulse variations. The first filling pulse used in this investigation were chosen short enough to not completely fill the electronic band-like states at an extended defect, should X be related to an extended defect. The

filling pulse widths used in the DLTS measurement were 10ms, 20ms, 30ms and 40ms with a bias voltage of -10V and a filling pulse voltage of 9.99V up from negative bias. Despite careful and abundant investigation, there was no evidence of peak-broadening or change in amplitude. This leads to the conclusion that X is probably not related to an extended defect and must therefore have point defect characteristics.

In an attempt to investigate surface states and rule out that X and/or Y in Fig.7.18 come from eventual defects close to the surface and are in fact not present in the bulk, DLTS investigation with a variation of the filling pulse voltage was done. The typical voltage used for all standard DLTS temperature spectra was -10V. This voltage allows investigation of traps in the depth of up to $3\mu\text{m}$. Changing the pulse voltage changes the depth to which defects can be discovered and allows to make a depth profile of the defects in the sample. In order to do so, voltages ranging from -3V to -20 have been used. The resulting DLTS plots showed no change in X or Y. This leads to the conclusion that X and Y are in fact uniformly distributed point defects of the bulk material.

In summary, the new defect X appears in all samples (including the reference series X460) and has a smaller electron capture cross section than $Z_{1/2}$. The peak in the DLTS plot coming from X is shifted to higher temperatures, which means that it is deeper in the band gap and therefore has a higher activation energy than $Z_{1/2}$. The concentration is generally higher and increases with oxidation time and temperatures. Despite this, the expected increase in lifetime is still maintained and is larger for higher oxidation times and temperatures. Extensive research lead to no references of these new defects X and Y in the literature or any publications. All of this lead to the conclusion, that X is in fact a new defect.

In order to learn more about the defect X, a simulation was used to see if theoretical calculations, given the properties determined from the DLTS measurements, fit the experimental results of the TRPL lifetime measurements. Additionally this simulation was used to give an approximation of the size of the hole capture cross section.

The simulation used for this purpose was created by I.Booker. The theoretical background for the TRPL measurement simulation is based on the carrier dynamic simulations done by Klein et al. [35].

For the simulation to work, several assumptions regarding X have been made based on the experimental findings:

- X is a new defect and not related to $Z_{1/2}$
- X is a single level
- X should have a small hole capture cross section ($< 2 \times 10^{-14}\text{cm}^2$) to not counteract the increase in lifetime due to $Z_{1/2}$ reduction
- $Z_{1/2}$ concentration is below the detection limit of the DLTS equipment (10^{11}cm^{-3})

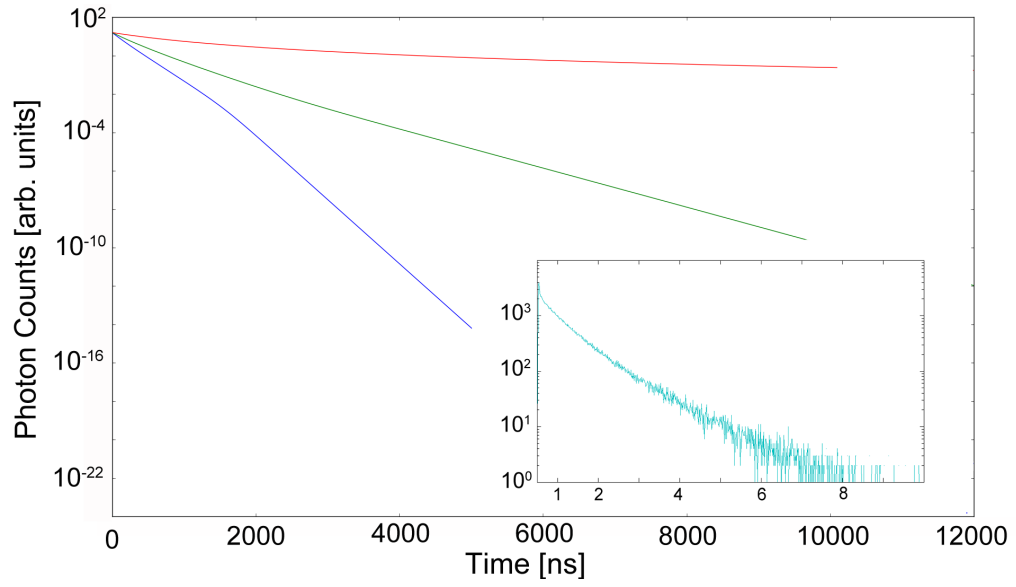
- Variation of the X concentration should only have a small effect on the PL lifetime

To find the a good approximation for σ_s the response of PL lifetime and signal over time has been calculated for three different hole capture cross sections $\sigma_s = 10^{-17} \text{cm}^2$, $6 \times 10^{-15} \text{cm}^2$ and $2 \times 10^{-14} \text{cm}^2$. The transient in Fig.7.20(a) decays too slow or too fast, depending on the σ_s used in the calculation, compared to the measured PL intensity decay shown in the inset. Following from the measurements, the PL intensity should decrease by about three orders of magnitude within the first $3\mu\text{s}$. The simulation shows that a σ_s of about 10^{-15}cm^2 reproduces the actual transient the best. The simulation of the PL lifetime over time in Fig.7.20(b) also proves $\sigma_s = 6 \times 10^{-15} \text{cm}^2$ to be the best guess for the hole capture cross section. Lesser or greater values for σ_s result in unphysical behavior or abnormally high lifetimes, respectively. The simulation results in Fig.7.20 are without regard for the assumption that the PL lifetime may not vary much with the X concentration.

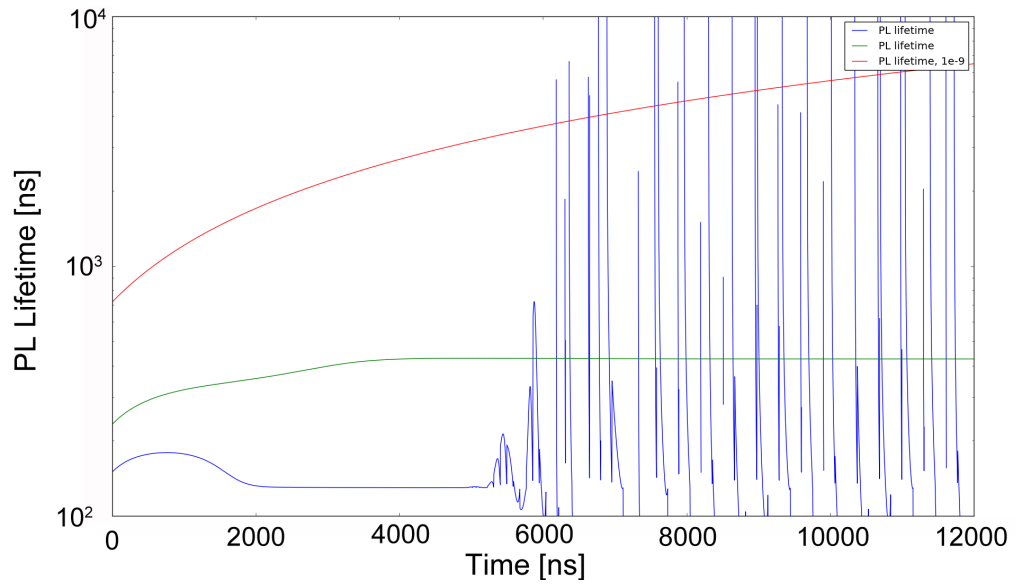
The variation of the PL intensity transient and lifetime over measure time with X concentration was also calculated for various σ_s . The X concentration variations represent the maximum and minimum values determined from the DLTS plots. The resulting dependencies are shown in Fig.7.21(a) and Fig.7.21(b).

As mentioned in the assumptions, the concentration should only have a small effect on the lifetime (and also the PL transient). As apparent from Fig.7.21(a), there is hardly any change in the transient for different concentrations for a very small σ_s in the order of 10^{-17}cm^2 . The PL lifetime dependence from the X concentration for two values σ_s is shown in Fig.7.22(a) and Fig.7.22(b).

The simulated PL lifetime should increase with measuring time in about the same magnitude as the measured lifetime and concentration variations should have little effect on it. Both figures deliver the same conclusion as Fig.7.21(a) and Fig.7.21(b) thus validating the assumption of σ_s being in the order of 10^{-17}cm^2 . The results of Fig.7.20, however, lead to the assumption that σ_s is in the order of 10^{-15}cm^2 . Thus far, it can only be said that the hole capture cross section should lie between these two values. Further simulations and measurements are necessary to gain better knowledge of these new defects.

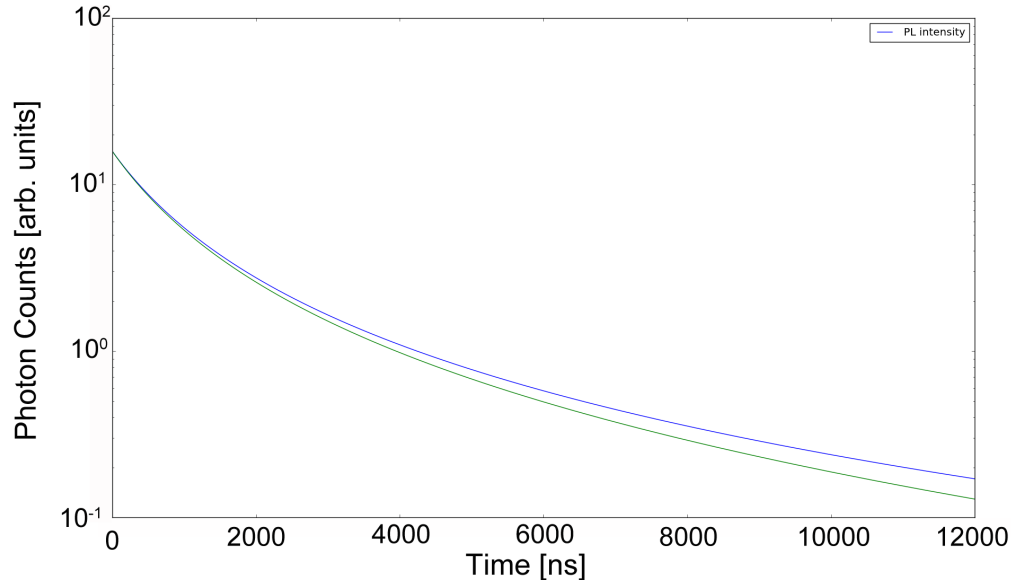


(a) Simulated PL transient for three different hole capture cross section.

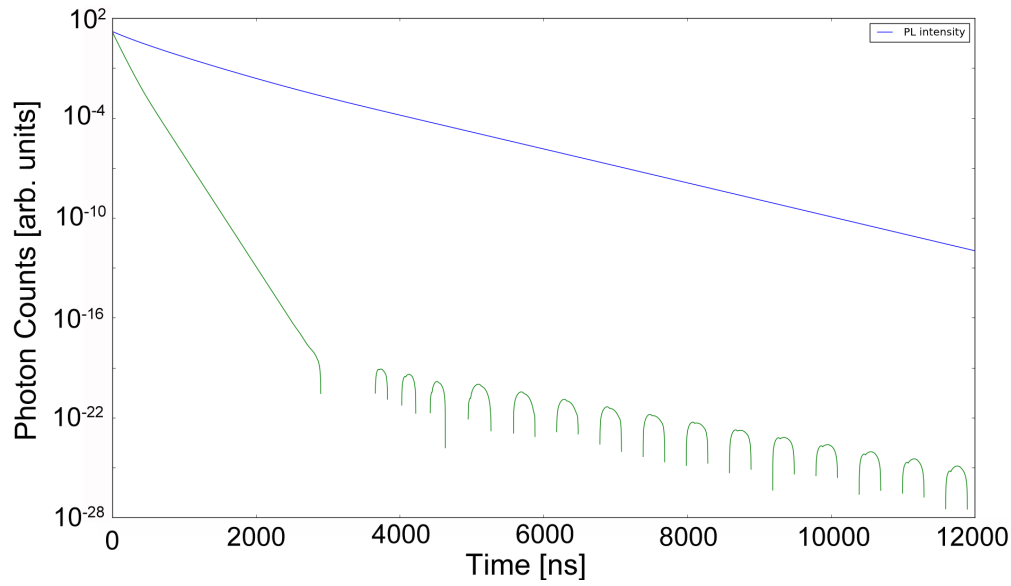


(b) Simulated PL lifetime for three different hole capture cross section. The high peaks at the end of the blue line are artifacts from the simulation

Figure 7.20: Simulation of PL transient and lifetime for three different hole capture cross sections. Blue line: $\sigma_s = 2 \times 10^{-14} \text{cm}^2$; green line $\sigma_s = 6 \times 10^{-15} \text{cm}^2$; red line: $\sigma_s = 1 \times 10^{-17} \text{cm}^2$

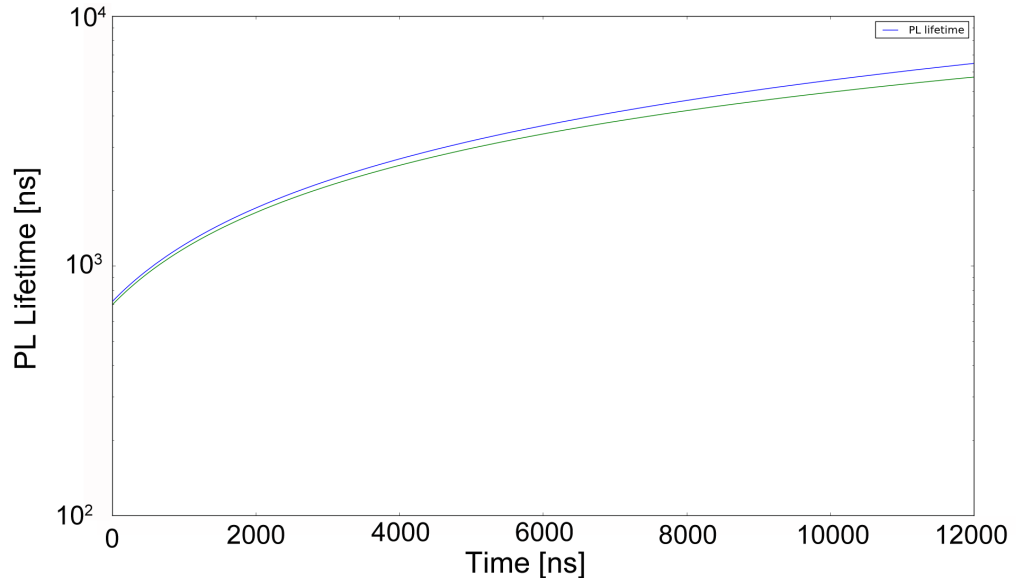


(a) Dependence of the simulated transient with a hole capture cross section of $\sigma_s = 1 \times 10^{-17} \text{ cm}^2$ with variation of the X concentration

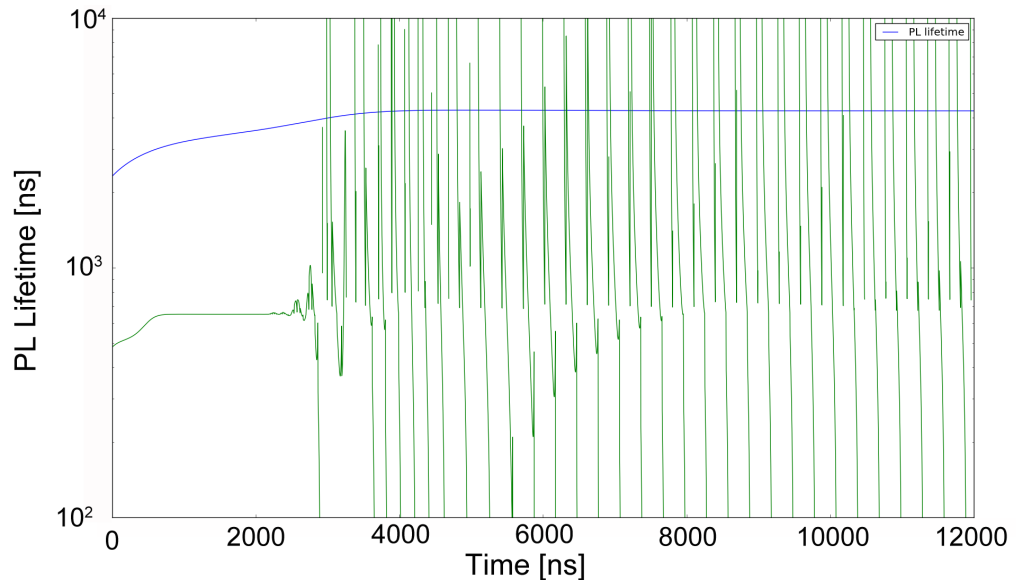


(b) Dependence of the simulated transient with a hole capture cross section of $\sigma_s = 6 \times 10^{-15} \text{ cm}^2$ with variation of the X concentration

Figure 7.21: Effect of the X concentration on the simulated PL transient for a large and a small hole capture cross section. The X concentrations are 3×10^{13} (blue line) and 2×10^{14} (green line).



(a) Dependence of the simulated lifetime with a hole capture cross section of $\sigma_s = 1 \times 10^{-17} \text{cm}^2$ with variation of the X concentration



(b) Dependence of the simulated lifetime with a hole capture cross section of $\sigma_s = 1 \times 10^{-17} \text{cm}^2$ with variation of the X concentration

Figure 7.22: Effect of the X concentration on the simulated PL transient for a large and a small hole capture cross section. The X concentrations are 3×10^{13} (blue line) and 2×10^{14} (green line).

Conclusion

The investigation of carrier lifetimes and defects before and after thermal oxidation delivered some unexpected results. The lifetime before oxidation showed a peculiar dependence on the temperature and a higher value at 200K. Although an increase in lifetime was present after the oxidation and the higher lifetime at 200K vanished, the dependence of the lifetime on the temperature remained, both of which can not be explained by the effect $Z_{1/2}$ alone [34].

Thermal oxidation was carried out at various temperatures including a very high temperature of 1500°C (very high compared to the temperatures usually used in these kind of experiments). A direct comparison of the Al_2O_3 furnace with the quartz furnace was not possible because the ordered quartz furnace capable of withstanding higher temperatures did not arrive in time.

Two new defects, labeled X and Y, appeared in the DLTS spectrum and which could not be related to any defects described in the literature or publications. The concentration of X increased with lifetime and from simulations it seems that X is a hole trap. Further investigation is needed to determine the nature and detailed properties of these new defects. This was not possible at the time, due to shortcomings of the equipment, like the incapability of measuring hole traps with the given DLTS set up, and lack of time.

Finally, the anomalous behavior of the X460 material could still not be explained, with the given experimental opportunities.

It is to say, that the results of this work leave much room for further experiments, more detailed simulations and theories about the nature and properties of defects in 4H-SiC.

List of Figures

2.1	Si-C Bilayer	4
2.2	Stacking sequence of 3C, 2H, 4H and 6H in the [1120] plane from [4]	5
2.3	Temperature dependence of the thermal conductivity	8
2.4	Hexagonal Brillouin zone and band structure of 4H-SiC.	10
2.5	Temperature and doping concentration dependence of the electron mobility in 4H-SiC from [55].	12
2.6	Various recombination processes depicted in a simple band model.	14
2.7	Impact ionization versus electric field strength [5].	16
3.1	Simple band model to demonstrate the various energy positions of defect states energy bands and the Fermi level from [54]	21
3.2	Calculated Temperature dependence of the intrinsic carrier concentration for Diamond, Si, 3C-SiC, 4H-SiC and 6H-SiC from [54]	23
3.3	Several kind of point defects in a crystal lattice [58].	24
3.4	Generation and recombination of carriers via deep levels in the band gap [58].	25
3.5	Two DLTS (see section 5.2) spectra observed in a 4H SiC diode. The measurements were performed (a) with a pulse width of $100\mu s$ and (b) with a pulse width of 50 ns and illumination with light $\lambda \approx 470nm$ from a GaN LED before each filling pulse. The pulse height was 9.9 V and the reverse bias -9.9V in both cases. Shown as an inset is the configuration-coordinate diagram for the center U_i where $i = 1, 2$ [21].	27
3.6	Schematic level scheme for carrier capture and emission at the $Z_{1/2}$ defect. The three charge states of $Z_1/Z_2(-, 0, +)$ are indicated, resulting in two transitions: 1 for $(-/0)$ and 2 for $(0/+)$. Transitions due to carrier capture or emission are indicated by solid or dashed arrows, respectively, with corresponding trap depths E_1 and E_2 . The net carrier capture rate for each transition is indicated by the R_{nj} and R_{pj} . [34]	27

4.1	Typical DLTS Plot with majority and minority carrier traps. The height of the peaks corresponds to the trap concentration [22].	30
4.2	Fit of the three SiC oxidation models, Deal-Grove, Si-emission model and Si-C-emission model, to experimental results [22].	32
4.3	Schematic model of the mechanism behind the reduction of $Z_{1/2}$ and $EH_{5/6}$ defect concentration by thermal oxidation [29].	33
5.1	Typical DLTS Plot with majority and minority carrier traps. The height of the peaks corresponds to the trap concentration [16].	39
5.2	Formation of a Schottky contact and the energy levels involved.	40
5.3	Pulse sequence during a DLTS measurement. From zero bias with capturing dominating a reverse bias is applied and emission becomes dominant. After the pulse the system returns to the steady state resulting in a transient [58].	42
5.4	The principle of the rate window in DLTS measurements [58].	44
5.5	Another illustration of the rate window concept. The lower part shows a typical activation energy plot and the upper part the equivalent response of the DLTS system [58].	45
7.1	TRPL lifetime mapping of the as-grown x511 samples. Each data point represents the fitted lifetime value from a lifetime transient measurement at this point at room temperature. The samples in the first row are from left to right x511-1, x511-2 and in the second row x511-3, x511-4, x511-5, x511-6, x511-7, x511-8, x511-9.	52
7.2	TRPL lifetime mapping of the as-grown x514 samples. Each data point represents the fitted lifetime value from a lifetime transient measurement at this point at room temperature. The samples used in this work are indicated.	52
7.3	Experimental cycle of the samples.	54
7.4	TRPL lifetime mapping of the oxidized samples. Each data point represents the fitted lifetime value from a lifetime transient measurement at this point at room temperature. The samples in the first row from left to right are x511-6, x511-9 and x514-7. The samples in the second row are x511-2 and x511-1.	55
7.5	TRPL lifetime mapping of the oxidized samples. Each data point represents the fitted lifetime value from a lifetime transient measurement at this point at room temperature. The samples from left to right are x511-8, x511-7 and x514-5, x514-D and x514-7.	56

7.6	TRPL lifetime mapping of the oxidized samples. Each data point represents the fitted lifetime value from a lifetime transient measurement at this point at room temperature. The samples from left to right are x511-13, x511-15.	56
7.7	Minority carrier lifetimes after the oxidation according to Table 7.1. The markings represent the lifetime of the sample averaged over the whole sample surface. The lines connecting the markings are guides to the eyes.	57
7.8	Oxide thicknesses after oxidation. The Markings represent the average thickness over the sample surface as measured by interferometry. The lines are fits by a power law of the form $y = Ax^b$. (T1200: A=0.013 B=0.547; T1300: A=0.011 B=0.555; T1400: A=0.183 B=0.249; T1500: A=0.214 B=0.272)	57
7.9	Absolute and relative lifetime after the oxidation. The lines connecting the data points are guides to the eyes. Full markings and lines represent the absolute values, while empty markings and dotted lines are relative values. The relative lifetimes was calculated simply by dividing the absolute lifetime after the oxidation by the as-grown lifetime.	59
7.10	The lifetime of the reference series compared to X511 and X514. Full markings and lines represent the absolute lifetimes from this work. Empty markings and dotted lines refer to the X460 series. The peculiar behavior of X460 at 1400°C (red dotted line) remains unexplained.	59
7.11	Relative lifetime increase of the X460 series. Like in Fig.7.10 the relative lifetime also shows a peculiar behavior at an oxidation temperature of 1400°C.	60
7.12	Representative room temperature PL spectrum of an unoxidized sample (X511-8). The spectrum shows three distinct peaks. Peak B is a result of laser artifacts, peak A is the band edge emission and peak C is of unknown origin and can only be speculated to be related to deep levels [39].	61
7.13	Representative PL spectra of an unoxidized sample (X511-8) at temperatures from 82K to 400K. For visual clarity, the spectra are separated by a factor of 10 each. The band edge peak separates in two peaks as the temperature decreases from room temperature and a new peak arises below 120K.	62
7.14	PL spectra of an oxidized sample (X511-8) at various temperatures. The oxidized sample shows fewer and smaller peaks compared to the as-grown state in Fig.7.13. The arrows indicate the maximum-fit lifetimes at the respective wavelengths and temperatures. Peaks without indication had too small signals for the lifetime to be measured reliably.	63

7.15	PL transients of unoxidized samples X511-8 and X514-2 with double logarithmic scale. Both show a sudden increase in lifetime at 200K and multi exponential behavior	64
7.16	Measured temperature dependence of the PL lifetime (open squares) compared to the simulated behavior (solid circles) [35]	66
7.17	PL decay transients at various temperatures of X511-8 after oxidation. The sudden lifetime increase and multi exponential behavior have disappeared after the oxidation.	66
7.18	DLTS plot of X511-13 as-grown (black lines) compared to after the oxidation (red lines) with three different rate windows at the same relation. The value of the rate windows are shown in the legend, with the smallest rate window being on the high temperature side.	67
7.19	Concentration of the new defect X over oxidation time for three oxidation temperatures. Missing data points could not be acquired due to heavy noise in the DLTS signal of some samples.	68
7.20	Simulation of PL transient and lifetime for three different hole capture cross sections. Blue line: $\sigma_s = 2 \times 10^{-14} \text{cm}^2$; green line $\sigma_s = 6 \times 10^{-15} \text{cm}^2$; red line: $\sigma_s = 1 \times 10^{-17} \text{cm}^2$	71
7.21	Effect of the X concentration on the simulated PL transient for a large and a small hole capture cross section. The X concentrations are 3×10^{13} (blue line) and 2×10^{14} (green line).	72
7.22	Effect of the X concentration on the simulated PL transient for a large and a small hole capture cross section. The X concentrations are 3×10^{13} (blue line) and 2×10^{14} (green line).	73

List of Tables

2.1	General Properties of Si, GaN and various polytypes of SiC. Data taken from [17], [50], [19], [33]	7
2.2	Electronic Properties of Si, GaN and various polytypes of SiC. Data taken from [17], [50], [19], [11]	9
7.1	Label, type of furnace and oxidation temperature and time used for the samples of this work as well as the reference samples. The oxidation time given in the table excludes the heating up and cooling down times.	50
7.2	As-grown mean lifetime, doping concentration and $Z_{1/2}$ oxidation temperature T_{ox} and time t_{ox} and electron capture cross section σ_n of the samples used in the experiments	51
7.3	Lifetime of oxidized samples τ_{ox} , relative lifetime increase τ_{rel} , density and electron capture cross section of the new defect N_T and σ_T and oxide thickness d_{ox} .	51

Bibliography

- [1] R. K. Ahrenkiel. Measurement Of Minority-Carrier Lifetime By Time-Resolved Photoluminescence. *Solid State Electronics*, 35(3):239–250, 1992.
- [2] F. Allerstam, H. Ö. Ólafsson, G. Gudjónsson, D. Dochev, and E. Ö. Sveinbjörnsson. *A strong Reduction in the Density of Near-Interface Traps at the SiO₂/4H-SiC Interface by Sodium enhanced Oxidation*, volume 101. 2007.
- [3] A. Taylor and R. M. Jones. *Silicon Carbide - A High Temperature Semiconductor*. Pergamon Press: Oxford, 1960.
- [4] T. Ayalew. *SiC Semiconductor Devices - Devices, Modeling, and Simulation*. PhD thesis, TU Wien, 2004.
- [5] B. Jayant Baliga. *Silicon Carbide Power Devices*. World Scientific, 2005.
- [6] J. Bardeen. *Surface States and Rectification at a Metal Semi-Conductor Contact*, volume 71. 1947.
- [7] F. Bechstedt, P. Käckell, A. Zywietz, K. Karch, B. Adolph, K. Tenelsen, and J. Furthmüller. Polytypism and Properties of Silicon Carbide. *Phys. Stat. Sol. (b)*, 202(35), 1997.
- [8] M. Bockstedte, A. Mattausch, and O. Pnkratov. *Silicon Carbide Recent Major Advances*. Springer, Berlin, 2003.
- [9] I.D. Booker, J. Hassan, A. Hallen, E.Ö. Sveinbjörnsson, O. Kordina, and J.P. Bergman. Comparison of Post-Growth Carrier Lifetime Improvement Methods for 4H-SiC Epilayers. Presentation ICSCRM2011, 2011.
- [10] L. J. Brillson. Surface Photovoltage Measurements and Fermi Level Pinning: Comments on Development and Confirmation of the Unified Model for Schottky Barrier Formation and MOS Interface States on III-V Compounds. *Thin Solid Films*, 89, 1982.

- [11] E. A. Burgermeister. Thermal Conductivity and Electrical Properties of 6H Silicon Carbide. *Journal Of Applied Physics*, 50(9), 1979.
- [12] N. Churcher, K. Kunc, and V. Heine. Calculated Ground-State Properties of Silicon Carbide. *Journal Of Physics C: Solid State Physics*, (19):4413–4426, 186.
- [13] A. G. Chynoweth. Ionization Rates for Electrons and Holes in Silicon. *Physical Review*, 109(5), 1958.
- [14] K. Danno and T. Kimoto. Deep Levels in Electron-Irradiated n- and p-type 4H-SiC Investigated by Deep Level Transient Spectroscopy. *Material Science Forum*, 556-557:331–334, 2007.
- [15] B. E. Deal and A. S. Grove. General Relationship for the Thermal Oxidation of Silicon. *Journal Of Applied Physics*, 36, 1965.
- [16] M. A. Gad and J. H. Evans-Freeman. High Resolution Minority Carrier Transient Spectroscopy of Si/SiGe/Si quantum wells. *Journal Of Applied Physics*, 92:5252–5258, 2002.
- [17] Y. Goldberg, M. E. Levinstein, and S. L. Rumyantsev. *Properties of Advanced Semiconductor Materials GaN, AlN, SiC, BN, SiC, SiGe*. Wiley, 2001.
- [18] M. Grundmann. *The Physics of Semiconductors*. Springer, 2006.
- [19] G. L. Harris. *Properties of Silicon Carbide*. Institution of Electrical Engineers, 1995.
- [20] T. Hayashi, K. Asano, and J. Suda. Temperature and injection level dependencies and impact of thermal oxidation on carrier lifetimes in p-type and n-type 4h-sic epilayers. *Journal of Applied Physics*, 109.
- [21] C. G. Hemmingsson, N. T. Son, A. Ellison, J. Zhang, and E. Janzén. Negative-U Centers in 4H Silicon Carbide. *Physical Review B*, 58(16), 1998.
- [22] Y. Hijikata, H. Yaguchi, and S. Yoshida. A Kinetic Model of Silicon Carbide Oxidation Based on the Interfacial Silicon and Carbon Emission Phenomenon. *Applied Physics Express*, 2(021203), 2009.
- [23] T. Hiyoshi and T. Kimoto. Reduction of Deep Levels and Improvement of Carrier Lifetime in n-Type 4H-SiC by Thermal Oxidation. *Applied Physics Express*, 2(041101), 2009.
- [24] A. Hopcroft. What is the Young's Modulus of Silicon? *Journal of Microelectromechanical Systems*, 19(2), 2010.

-
- [25] R. P. Joshi. Monte Carlo Calculations of the Temperature and Field dependent Electron Transport Parameters for 4H-SiC. *Journal Of Applied Physics*, 78(5518-5521), 1995.
- [26] C. H. Carter Jr, V. F. Tsvetkov, R. C. Glass, D. Henshall, M. Brady, G. Müller, O. Kordina, K. Irvine, J. A. Edmond, H.-S. Kong, R. Singh, S. T. Allen, and J. W. Palmour. Progress in SiC: From Material Growth to Commercial Device Development. *Material Science and Engineering*, B61-62:1–8, 1999.
- [27] B. Kaczer, H.-J. Im, and J. P. Pelz. Direct Observation of Conduction-Band Structure of 4H- and 6H-SiC using Ballistic Electron Emission Microscopy. *Physical Review B*, 57(7), 1998.
- [28] M. Kanaya, J. Takahashi, and Y. Fujiwara. Controlled Sublimation Growth of Single Crystalline 4H-SiC and 6H-SiC and Identification of Polytypes by X-Ray Diffraction. *Applied Physics Letters*, 58, 1991.
- [29] K. Kawahara, J. Suda, and T. Kimoto. Analytical Model for Reduction of Deep Levels in SiC by Thermal Oxidation. *Journal Of Applied Physics*, 111(053710), 2012.
- [30] T. Kimoto. Sic technologies for future energy electronics. *Symposium on VLSI Technology Digest of Technical Papers*, 2010.
- [31] T. Kimoto, K. Hashimoto, and H. Matsunami. *Japan Journal of Applied Physics*, 42:7249, 2003.
- [32] T. Kinoshita, K. M. Itoh, J. Muto, M. Schadtand G. Pensl, and K. Takeda. Calculation of the Anisotropy of the Hall Mobility in n-type 4H- and 6H-SiC. *Material Science Forum*, 264-268:295–298, 1998.
- [33] K. Kamitani, M. Grimsditch, and J. C. Nipko. The Elastic Constants of Silicon Carbide: A Brillouin-Scattering Study of 4H and 6H SiC Single Crystals. *Journal Of Applied Physics*, 82(6):3152 – 3154, 1997.
- [34] P. B. Klein. Carrier Lifetime Measurement in 4H-SiC Epilayers. *Journal Of Applied Physics*, 103(033702), 2008.
- [35] P. B. Klein. Identification and Carrier Dynamics of the dominant Lifetime limiting Defect in n-4H-SiC Epitaxial Layers. *Phys. Stat. Sol. A*, 206(10):2257–2272, 2009.
- [36] P. B. Klein and B. V. Shanabrook. Lifetime-limiting Defects in n-4H-SiC Epilayers. *Applied Physical Letters*, 88, 2006.

- [37] J. M. Knaup, P. Deak, and T. Frauenheim. Theoretical Study of the Mechanisms of Dry Oxidation of 4H-SiC. *Phys. Rev. B*, 71.
- [38] O. Kordina. *Growth and Characterisation of Silicon Carbide Power Device Material*. PhD thesis, Linköpings University, 1994.
- [39] B. Krishnan, S. K. Chanda, and Y. Koshka. Properties of Different Room-temperature Photoluminescence Bands in 4H-SiC Substrates Investigated by Mapping Techniques. *Material Science Forum*, 556-557, 2007.
- [40] D. V. Lang. Deep-level Transient Spectroscopy: A new method to characterize traps in semiconductors. *Journal Of Applied Physics*, 45(7), 1974.
- [41] R. T. Leonard. 100 mm 4H-SiC Wafers with zero Micropipe Density. *Material Science Forum*, 600 - 603:7 – 10, 2009.
- [42] I. Lindau and T. Kendelewicz. Schottky Barrier Formation on III-V Semiconductor Surfaces: Schottky Barrier Formation on III-V Semiconductor Surfaces: A Critical Evaluation. *CRC Critical Review in Solid State and Material Science*, 13, 1986.
- [43] H.-S. Liu, X.-Y. Fang, W.-L. Song, Z.-L. Hou, R. Lu, J. Yuan, and M.-S. Cao. Modification of the Band Gap of β -SiC by N-Doping. *Chinese Physics Letters*, (26 067101), 2009.
- [44] H. Z. Massod. *Journal Of Electrochemical Society*, 1985.
- [45] D. T. Morelli, J. P. Heremans, and C. P. Beetz. Institute of physics conference series n137. In *Silicon Carbide and Related Materials Eds. Spencer M.G.*, 1993.
- [46] D. T. Morelli, J. P. Heremans, C. P. Beetz, W. S. Yoo, and H. Matsunami. Phonon-electron Scattering in Single Crystal Silicon Carbide. *Applied Physical Letters*, 63(3143), 1993.
- [47] S. Nakashima and H. Harima. Characterization of Structural and Electrical Properties in SiC by Raman Spectroscopy. *Institute of Physics Conference Series*, pages 269–272, 1996.
- [48] K. C. Nomura and J. S. Blakemore. Decay of Excess Carriers in Semiconductors II. *Physical Review*, 121(3), 1961.
- [49] J. W. Palmour, H.-S. Kong, and R. F. Davis. Characterization of Device Parameters in High-Temperature Metal-Oxide-Semiconductor Field Effect Transistors in β -SiC Thin Films. *Journal Of Applied Physics*, 64:2168, 1988.

-
- [50] G. Pensl. Sic material properties. *International Journal of High Speed Electronics and Systems*, 15(4):705 – 745, 2005.
- [51] D. Perone. *Process and Characterization Techniques on 4H-Silicon Carbide*. PhD thesis, Politecnico di Torino, 2007.
- [52] A. Qteish, R. J. Needs, and V. Heine. Polarization, Structural and Electronic Properties of SiC Polytypes. *Computational Material Science*, 2:389–394, 1994.
- [53] E. A. Ray. *Journal Of Applied Physics*, 103, 2008.
- [54] H. Romanus. *Siliziumkarbidelektronik - Technologische und Werkstoffwissenschaftliche Untersuchungen zur Metallisierung/Kontaktierung*. PhD thesis, TU Ilmenau, 2004.
- [55] M. Roschke and F. Schwierz. Electron Mobility Models for 4H, 6H, and 3C-SiC [mesfets]. *Electron Devices, IEEE Transactions on*, 48(7):1442 –1447, jul 2001.
- [56] H. J. Round. A note on Carborundum. *Electrical World*, 3:309 – 310, 1907.
- [57] W. J. Schaffer, G. H. Negley, K. G. Irvine, and J. W. Palmour. Conductivity Anisotropy in epitaxial 6H- and 4H-SiC. *Material Research Society Proceedings*, 339:595–600, 1994.
- [58] D. K. Schroder. *Semiconductor Material And Device Characterization*. Wiley-Interscience, 2006.
- [59] W. Shockley. Electrons, Holes and Traps. 1958.
- [60] W. Shockley and W. T. Read. *Phys. Rev.*, 87.
- [61] A. Slack. Thermal Conductivity of Pure and Impure Silicon, Silicon Carbide, and Diamond. *Journal Of Applied Physics*, 35(12), 1964.
- [62] A. B. Sproul. *Journal Of Applied Physics*, 76, 1994.
- [63] L. Storasta, H. Tsuchida, and T. Miyazawa. Enhanced Annealing of the $Z_{1/2}$ Defect in 4H-SiC Epilayers. *Journal Of Applied Physics*, 103(013705), 2008.
- [64] J. Tersoff. Recent Models of Schottky Barrier Formation. *Journal of Vacuum Science Technology B*, 3, 1985.
- [65] B. Thomas, W. Bartsch, and R. Stein. Properties and Suitability of 4H-SiC Epitaxial Layers Grown at Different CVD Systems for High Voltage Applications. *Material Science Forum*, 457-460:181–184, 2004.

- [66] A. R. Verma and P. Krishna. *Polymorphism and Polytypism in Crystals*. Wiley, 1966.
- [67] I. Vickridge, J. Ganem, Y. Hoshino, and I. Trimaille. Growth of SiO₂ on SiC by dry Thermal Oxidation: Mechanisms. *Journal Of Physics D: Applied Physics*, 40:6254 – 6263, 2007.
- [68] P.-S. Xu, C.-K. Xie, H.-B. Pan, and F.-Q. Xu. Theoretical Study on the Band Structure and Optical Properties of 4H-SiC. *Chinese Physics Letters*, (13 2126), 2004.
- [69] T. Yamamoto. *Material Science Forum*, 600-603(667), 2009.
- [70] Feng Yan, Xiaobin Xin, S. Aslam, Yuegang Zhao, D. Franz, J.H. Zhao, and M. Weiner. 4H-SiC UV Photo Detectors with large Area and very high specific Detectivity. *Quantum Electronics, IEEE Journal of*, 40(9):1315 – 1320, sept. 2004.
- [71] C. M. Zetterling. Process technology for silicone carbide devices. Docent Lecture available at: <http://web.it.kth.se/bellman/docs/ZetterlingDocentLecture.pdf>.
- [72] A. Zywietz, K. Arch, and F. Bechstedt. Influence of polytypism on thermal properties of silicon carbide. *Physical Review B*, 54(3):1791 – 1798, 1996.